Eruptive history of the Karoo lava flows and their impact on early Jurassic environmental change

M. Moulin, F. Fluteau, V. Courtillot, J Marsh, G. Delpech, X. Quidelleur, M. Gerard

AGU PUBLICATIONS

JGR

Journal of Geophysical Research: Solid Earth

RESEARCH ARTICLE
10.1002/2016JB013354

This article is a companion to *Moulin et al.* [2011] doi:10.1029/2011JB008210.

Key Points:
- We combine paleomagnetism and dating to study a 1500 m thick composite section (Drakensberg group) in Lesotho
- We show that the major part of the Drakensberg group was emplaced over a period as short as 250 kyr
- We propose a scenario connecting Karoo volcanism and the major environmental perturbations of the Early Jurassic

Supporting Information:
- Table S1

Correspondence to:
F. Fluteau,
fluteau@ipgp.fr

Citation:
Moulin, M., F. Fluteau, V. Courtillot, J. Marsh, G. Delpech, X. Quidelleur, and M. Gérard (2017), Eruptive history of the Karoo lava flows and their impact on early Jurassic environmental change, *J. Geophys. Res. Solid Earth*, *122*, 738–772, doi:10.1002/2016JB013354.

Received 13 JUL 2016
Accepted 2 JAN 2017
Accepted article online 4 JAN 2017
Published online 3 FEB 2017

Eruptive history of the Karoo lava flows and their impact on early Jurassic environmental change

M. Moulin[1], F. Fluteau[1], V. Courtillot[1], J. Marsh[2], G. Delpech[3,4], X. Quidelleur[3,4], and M. Gérard[5]

[1]Institut de Physique du Globe de Paris, Sorbonne Paris Cité, Université Paris Diderot, Paris, France, [2]Department of Geology, Rhodes University, Grahamstown, South Africa, [3]Laboratoire GEOPS, Université Paris-Sud, Orsay, France, [4]CNRS, Orsay, France, [5]IMPMC, Université Pierre et Marie Curie, IRD, Paris, France

Abstract This paper reports new paleomagnetic and geochronologic data from a ~1500 m thick composite section belonging to the Drakensberg group, the thickest remnant of the Karoo lavas in Northern Lesotho. Flow-by-flow analysis of paleomagnetic directions reveals 21 magnetic directional groups, corresponding to single eruptive events, and 16 individual lava flows. The new age determinations of lava flows range from 180.1 ± 1.4 to 182.8 ± 2.6 Ma. These data, combined with previous results, allow us to propose that the main part of the Drakensberg group and the Karoo intrusive complex dated around 181–183 Ma may have been erupted over a period as short as 250 kyr and may have coincided with the two main phases of extinction in the Early Toarcian. This scenario agrees well with the discontinuous rhythm of environmental and biotic perturbations in the Late Pliensbachian-Toarcian interval.

1. Introduction

Sixteen large igneous provinces (LIPs), comprising continental flood basalts (CFBs) and oceanic plateaus, have been emplaced during the Phanerozoic [e.g., *Courtillot and Renne*, 2003]. The likelihood of a cause-and-effect link between mass extinctions and LIPs has been highlighted by the discovery of the close temporal relationship between these phenomena [*Rampino and Stothers*, 1988; *Courtillot*, 1994; *Hallam and Wignall*, 1997; *Courtillot and Renne*, 2003; see recent review in *Courtillot and Fluteau*, 2014; *Courtillot et al*., 2015]. Although details of this relationship remain controversial, it is generally proposed that massive injection of gases (mainly SO_2 and CO_2) into the atmosphere during emplacement of LIPs could have led to major environmental changes, resulting in mass extinction. Two major processes are suggested: a direct release during lava flow emplacement [e.g., *Wignall*, 2001; *Courtillot and Renne*, 2003; *Chenet et al*., 2009] and an indirect release due to degassing induced by contact metamorphism in cases where magmas are intruded in C- or S-rich sedimentary layers [*Svensen et al*., 2004, 2007; *Ganino and Arndt*, 2009]. The huge amounts of SO_2 and CO_2 released into the atmosphere by CFB volcanism can influence the environment through two "opposite" processes acting on quite different timescales: (1) conversion of SO_2 initially injected into the stratosphere to sulfuric acid aerosols (H_2SO_4), resulting in atmospheric cooling [e.g., *Robock*, 2000]; and (2) long-term accumulation of CO_2 resulting in atmospheric warming [e.g., *McLean*, 1985]. However, details of the atmospheric and biotic consequences of gas release from flood basalt volcanism remain poorly understood.

Why are apparently similarly huge CFBs associated with very different levels of extinction severity? Could this be due to differences in height, size, and duration of eruptive column; composition of erupted gases; nature of erupted ashes; chemical composition of intruded crust; latitude of eruption; geography of continents and oceans; pre-eruption composition; and state of atmosphere? None of these allow unambiguous differentiation of one event from another. The estimated volumes of LIPs and extinction intensities are actually uncorrelated [e.g., *Wignall*, 2001; *Courtillot and Renne*, 2003]. *Svensen et al*. [2009] and *Ganino and Arndt* [2009] pointed out the role of metamorphic gases released when magmatism intruded organic-rich shale layers, evaporites, and limestone. Understanding of the eruptive dynamics, and notably of the detailed extrusion rate history, is certainly essential to determine the environmental and biotic impacts of flood basalt volcanism [e.g., *Bond and Wignall*, 2014; *Courtillot and Fluteau*, 2014, for recent reviews of the causes and effects of volcanism on mass extinctions].

Our working hypothesis is that the *tempo* of outpouring of huge amounts of magma over very short durations is the key feature of LIP volcanism: for the same numbers, sizes, and total volumes of flows, the

response of the coupled ocean/atmosphere system would be very different if flows erupted at intervals longer than the time needed for the ocean to re-equilibrate, or if it erupted in a faster sequence, leading to runaway effects. Testing this hypothesis requires a temporal resolution that was unattainable with current isotopic/geochronologic (K-Ar, $^{40}Ar/^{39}Ar$) methods. Many studies underline the "brevity" (geologically speaking) of LIP emplacement, on the order of a few million years: 2–4 Myr for the Deccan LIP [*Jerram and Widdowson*, 2005; *Chenet et al*., 2007], 6–10 Myr for the Siberian [*Ivanov et al*., 2005] and Parana-Etendeka [*Thompson et al*., 2001] LIPs, and ~4 Myr for the emplacement of the main part of the Karoo LIP [*Jourdan et al*., 2008]. Recently, studies based on U-Pb TIMS (thermal ionization mass spectrometry) ages on zircon crystals isolated from lavas, pyroclastic rocks, and sills have shown that the duration of emplacement of CFB was even shorter [*Svensen et al*., 2012; *Sell et al*., 2014; *Schoene et al*., 2015; *Burgess and Bowring*, 2015]. Indeed, *Schoene et al*. [2015] have shown that the emplacement of the Main Province of the Deccan CFB lasted ~750 kyr and began 250 kyr before the Cretaceous-Paleogene boundary. In the case of the Siberian CFB, *Burgess and Bowring* [2015] determined that two thirds of the ~4 million km^3 of magmas were emplaced over a period as short as 300 kyr, overlapping the end Permian mass extinction. But if volcanism and gas injection had taken place uniformly over such durations (even the shorter ones), one might have doubts on the ability of LIP emplacement to cause severe climatic change and biotic crises. However, paleomagnetic studies have revealed the very intermittent character of flood basalt volcanism [*Riisager et al*., 2003; *Knight et al*., 2004; *Chenet et al*., 2008, 2009]. For instance, *Chenet et al*. [2008, 2009] have shown that the Main Province of the Deccan traps (80% of the total volume of basalt) was erupted in a small number of very large (up to 20,000 km^3) and short-lived (~10 to 100 years) volcanic pulses that could have led to major environmental changes, resulting in the KT mass extinction. Further testing of the hypothesis requires a similarly detailed study of the eruptive dynamics of a CFB that has been associated with a second-order mass extinction. We have undertaken such a study, focusing on the Karoo-Ferrar CFB.

The emplacement of the Karoo-Ferrar CFB coincides with the second-order Pliensbachian-Toarcian (Pl-To) extinctions [*Pálfy and Smith*, 2000; *Guex et al*., 2001, 2012; *Courtillot and Renne*, 2003; *Sell et al*., 2014]. Still, the Pl-To crisis represents one of the most severe events affecting marine biota of the Mesozoic [*Sepkoski*, 1986]. It consisted of a succession of five or six extinctions of variable intensity occurring over a period of 10 Myr, from the lower Pliensbachian to the upper Toarcian [*Dera et al*., 2010; *Caruthers et al*., 2013]. The two most severe extinctions, during which several different groups of microfossils and macrofaunas [see *Dera et al*., 2010] were affected, occurred successively at the end Pliensbachian (*Spinatum*/*Tenuicostatum* biozone boundary) and during the Early Toarcian (*Tenuicostatum*/*Falciferum* (*Serpentinum*) biozones) [*Dera et al*., 2011; *Guex et al*., 2012]. The end Pliensbachian crisis coincides with a global regression event and a major global cooling, having possibly led to a short period of glaciation [*Guex et al*., 2012]. The end Pliensbachian and Early Toarcian have also witnessed major carbon cycle perturbations. A sharp negative carbon isotope excursion (CIE) is observed during the Early Toarcian in marine and continental organic matter, in carbonates of the Western Tethyan ocean [e.g., *Hesselbo et al*., 2000, 2007; *Jenkyns et al*., 2001; *Gomez et al*., 2008; *Hermoso et al*., 2009, 2012, 2013; *Suan et al*., 2010; *Jenkyns*, 2010], in polar regions [*Suan et al*., 2011], in the Panthalassa [Canada—*Caruthers et al*., 2011; Japan—*Kemp and Izumi*, 2014; Peru—*Guex et al*., 2012], and in the Neuquén Basin in Argentina [*Al-Suwaidi et al*., 2010]. It coincides with an oceanic anoxic event (Toarcian oceanic anoxic event) evidenced by black shale in European epeiric seas and western Tethyan margins, a major marine transgression and a phase of global warming reaching an acme during the *Falciferum* biozone [*McArthur et al*., 2000; *Bailey et al*., 2003; *Gomez et al*., 2008; *Suan et al*., 2008; *Dera et al*., 2009; *Suan et al*., 2010; *Krencker et al*., 2014].

The present paper describes the emplacement of the thickest remnant of the Karoo CFB in Northern Lesotho following the procedures and methods used by *Chenet et al*. [2008, 2009] for the Deccan CFB and results from a first section of the Karoo CFB at Naude's Nek in South Africa [*Moulin et al*., 2011]. We propose a synthesis of the whole body of information available for the Karoo province and its relation to Pliensbachian-Toarcian environmental and biotic perturbations.

2. Geological Background, Previous Results, and Description of the New Sections

2.1. The Karoo and Ferrar Provinces

The Karoo LIP consists of a complex series of separate lava flows, sills, and dykes over much of Southern Africa (Figure 1a). The Ferrar province forms an elongated extension of the Karoo in Antarctica. The main part of the

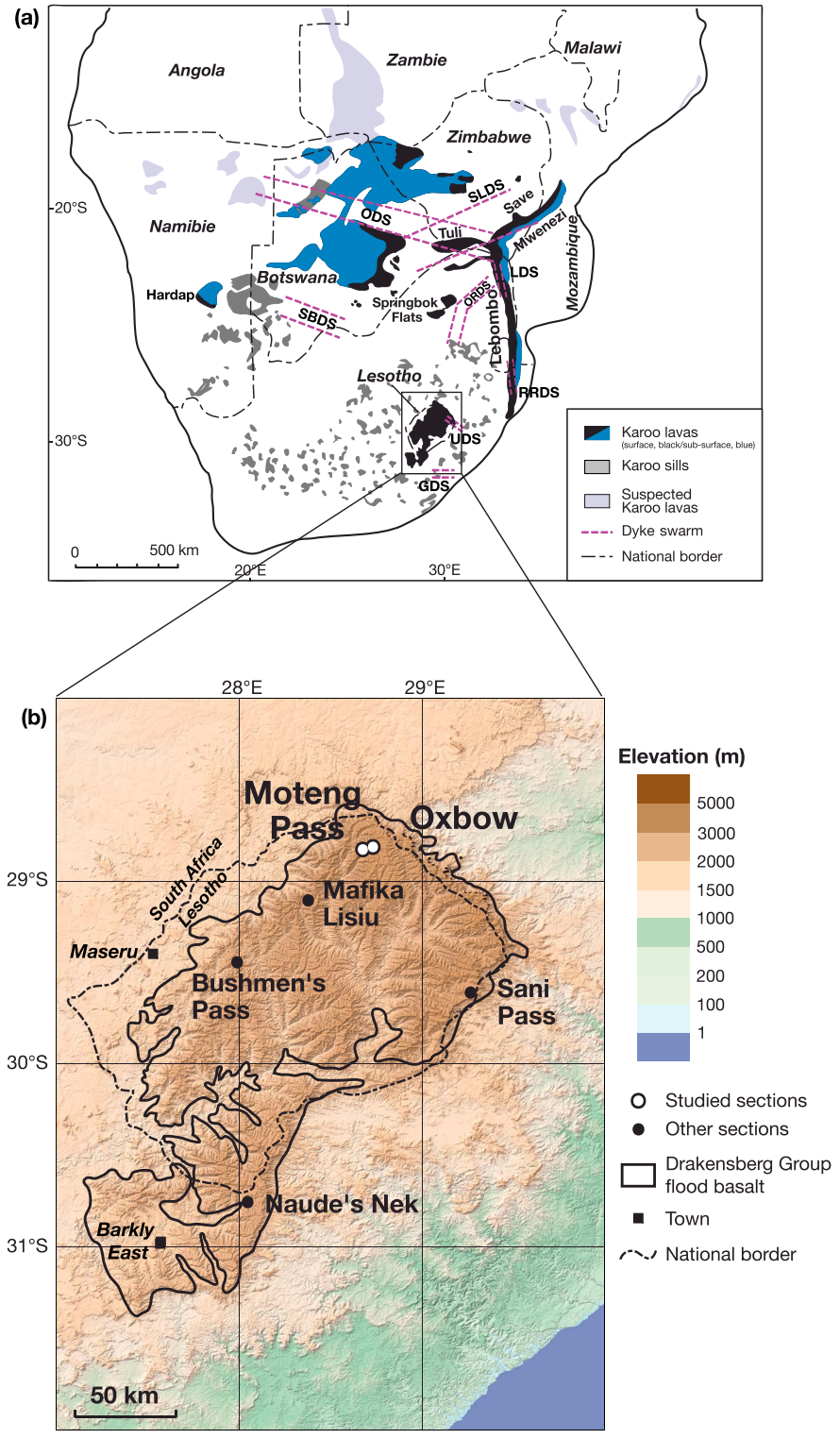

Figure 1. (a) Geological extent of the Karoo large igneous province in Southern Africa [modified after *Jourdan et al.*, 2008, and *Marsh et al.*, 1997; *Marsh* 2002]. ODS, Okavango dike swarm; SLDS, Save Limpopo dike swarm; LDS, Lebombo dike swarm; ORDS, Olifants River dike swarm; RRDS, Rooi Rand dike swarm; SBDS, south Botswana dike swarm; UDS, Underberg dike swarm and GDS, Gap dike swarm. (b) Topography of the Lesotho part of the Karoo lavas (Drakensberg group) with locations of the studied sections, Moteng Pass and Oxbow in Lesotho (white circles). The black circles represent other sections discussed in the paper (Sani Pass and Mafika Lisiu [*Kosterov and Perrin*, 1996]; Bushmen's Pass [*Prévot et al.*, 2003]; Naude's Nek [*Moulin et al.*, 2011]).

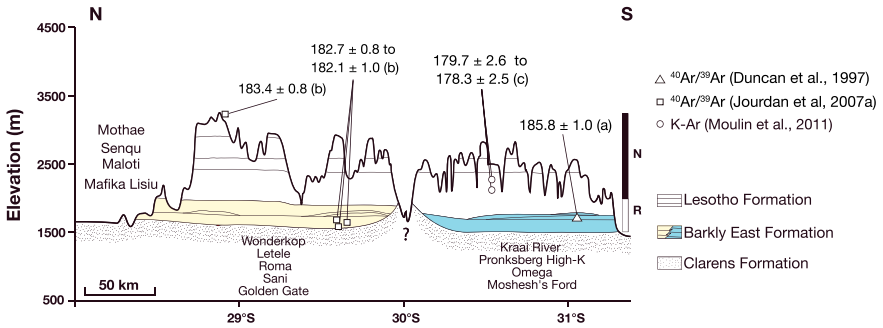

Figure 2. Geochemical stratigraphy, magnetic stratigraphy, and absolute ages of the Drakensberg group (Barkly East and Lesotho Formations). Geochemical magma types (units) are from *Marsh et al.* [1997]. Magnetic polarities are a synthesis from *Rehacek* [1995], *Kosterov and Perrin* [1996], *Prévot et al.* [2003], and *Moulin et al.* [2011]. (a) $^{40}Ar/^{39}Ar$ age (shown by triangle) (with 1σ total uncertainty) from *Duncan et al.* [1997] relative to 28.03 Ma for the FCT-3 flux monitor. (b) $^{40}Ar/^{39}Ar$ ages (shown by squares) from *Jourdan et al.* [2007a] relative to 1072 Ma for the Hb3gr flux monitor. (c) K-Ar ages (shown by circles) with 1σ total uncertainties from *Moulin et al.* [2011].

Karoo volcanic province was erupted within a ~3 Myr period (181–184 Ma) [*Jourdan et al.*, 2008] and overlaps the Late Pliensbachian-Early Toarcian environmental changes and biotic crisis [e.g., *Pálfy and Smith*, 2000; *Guex et al.*, 2012].

Volcanic remnants of the lower Jurassic Karoo province are characterized by numerous isolated outcrops [*Eales et al.*, 1984], mainly scattered in the southern part of Africa, from the north of South Africa to Zambia and Malawi (Figure 1a). The thickest volcanic sequence (about 1500 m) is found in Lesotho and South Africa, where it is formally known as the Drakensberg group (Figures 1a and 1b). Rock types are overwhelmingly basalts with almost indistinguishable tholeiitic compositions, but locally, other types (andesite, nephelinite, picrite, and rhyolite) may be encountered, mainly within the Lebombo monocline [*Eales et al.*, 1984; *Marsh et al.*, 1997] (Figure 1a). On the other hand, the Karoo LIP is characterized by the presence of a large network of doleritic sills and dykes that are particularly well developed in the main Karoo Basin [*Du Toit*, 1920; *Chevallier and Woodford*, 1999]. Giant dyke swarms intrude the sedimentary formations of the Karoo Supergroup to the south (in South Africa) and the Archean basement to the north (in Zimbabwe) [*Eales et al.*, 1984; *Le Gall et al.*, 2002] (Figure 1a). Ages and similarities in geochemical signature suggest that the Dronning Maud Land magmatic province in Antarctica (now separated from the African continent by the southwest Indian Ocean) is related to the Karoo province [*Brewer et al.*, 1996; *Duncan et al.*, 1997; *Marsh et al.*, 1997]. Karoo LIP magmas have chemical affinities and overlap in age with flood basalts of the Ferrar magmatic province encountered in Antarctica, Australia, and New Zealand [*Mortimer et al.*, 1995; *Duncan et al.*, 1997; *Elliot and Fleming*, 2000; *Riley and Knight*, 2001]. The original volume of the Karoo-Ferrar magmatic event is estimated at about ~2.5×10^6 km^3 [*Cox*, 1988; *Encarnacion et al.*, 1996], making it one of the largest Mesozoic LIPs associated with Gondwana breakup [*Duncan et al.*, 1997; *Riley and Knight*, 2001].

2.2. The Drakensberg Group

Our research program has been focused on the Drakensberg group, a plateau consisting of low-Ti tholeiitic basalt flows exposed mainly in Lesotho, and the thickest remnant of the Karoo LIP (Figures 1a and 1b). The lava flow succession is subdivided into two geochemical formations: the lower Barkly East Formation and the upper Lesotho Formation (Figure 2) [*Marsh et al.*, 1997]. The Barkly East Formation (less than 300 m thick) consists of thin discrete and heterogeneous geochemical units extending over small areas. The geochemical units of the Barkly East Formation found in the northern part of Lesotho (north of about 30°S) are not the same as those found in the southern part (Figure 2). The Lesotho Formation (more than 1300 m thick) is encountered all over Lesotho [*Marsh et al.*, 1997]. This formation comprises thicker chemical units that are less variable in composition than the Barkly East Formation. Paleomagnetic studies of the Drakensberg group [*Van Zijl et al.*, 1962a, 1962b; *Kosterov and Perrin*, 1996; *Hargraves et al.*, 1997; *Prévot et al.*, 2003; *Moulin et al.*, 2011, 2012] reveal a single magnetic reversal (from reverse to normal polarity) in the first geochemical unit of the Lesotho Formation (the Mafika Lisiu unit) (Figure 2). Because reversals were rather frequent during the Early Jurassic [e.g., *Ogg and Smith*, 2004], relatively brief emplacement (<1 Ma) of the Drakensberg group

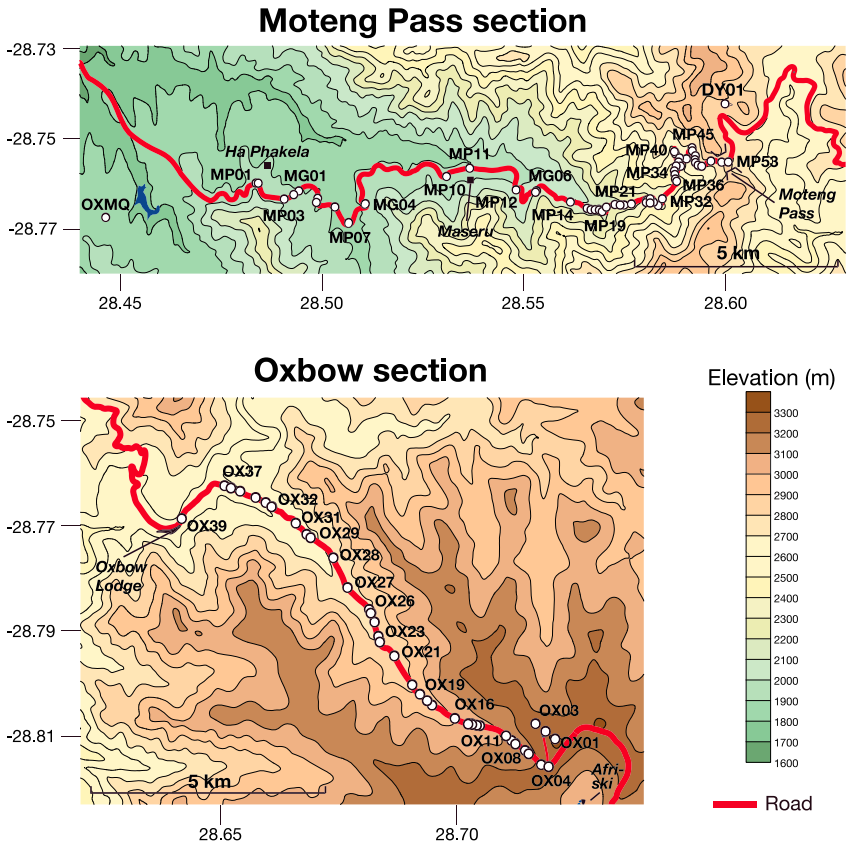

Figure 3. Maps showing the location of the 97 paleomagnetic sites (some sites not labeled) sampled along the Oxbow and Moteng Pass sections. Topographic maps are based on Shuttle Radar Topography Mission 2 (SRTM2) [*Rodriguez et al*., 2005].

is inferred. This short duration is consistent with an estimate of ~0.8 Ma suggested by *Jourdan et al*. [2007a] for the emplacement of the whole Lesotho LIP remnant (around 181.6 ± 0.4 Ma, relative to 1072 Ma for the Hb3gr flux monitor). A complex intrusive system within the sedimentary Karoo basin represents an important part of Karoo magmatism [*Galerne et al*., 2008; *Neumann et al*., 2011]. Analyses conducted on sills and dykes exposed at the surface or from drill cores revealed geochemical similarities with the Lesotho Formation [*Marsh and Eales*, 1984; *Mitha*, 2006; *Galerne et al*., 2008; *Neumann et al*., 2011], and high-resolution U-Pb TIMS on zircons from these sills yields consistent ages (of crystallization) ranging from 183.0 ± 0.5 to 182.3 ± 0.6 Ma [*Svensen et al*., 2012]. Two ages obtained by *Duncan et al*. [1997] ($^{40}Ar/^{39}Ar$ age) and more recently by *Moulin et al*. [2011] (K-Ar age) (see below) in the southern part of the Barkly East Formation are slightly (though marginally) older, suggesting the possibility of an earlier phase of volcanic activity, a few million years prior to the emplacement of the main volcanic phase [*Moulin et al*., 2011].

2.3. Previous Results From the Naude's Nek Section

Our first results, from an 800 m thick section of the Karoo LIP at Naude's Nek (NN) near the southern border of Lesotho, have been published by *Moulin et al*. [2011] (Figure 1b). In summary, our first age determinations (K-Ar Cassignol-Gillot technique) yielded a mean age of 179.2 ± 1.8 Ma for the major upper part of the volcanic sequence, in good agreement with previous studies [*Jourdan et al*., 2007a]. However, a sample from the lowermost unit suggested the presence of an older phase of volcanism at 184.8 ± 2.6 Ma. The Naude's Nek section has recorded a simple succession of reversed, transitional, and normal magnetic polarities. Directional groups (DGs) of lava flows with quasi-identical remanence directions indicate eruption durations too short to have recorded geomagnetic secular variation and hence are interpreted as single eruptive events (SEEs). Altogether, 19 DGs and 10 individual lava flows yield a sequence of 29 distinct directions. This could correspond to a total eruptive activity shorter than 3000 years (not including the amount of time elapsed between successive volcanic pulses). Particular

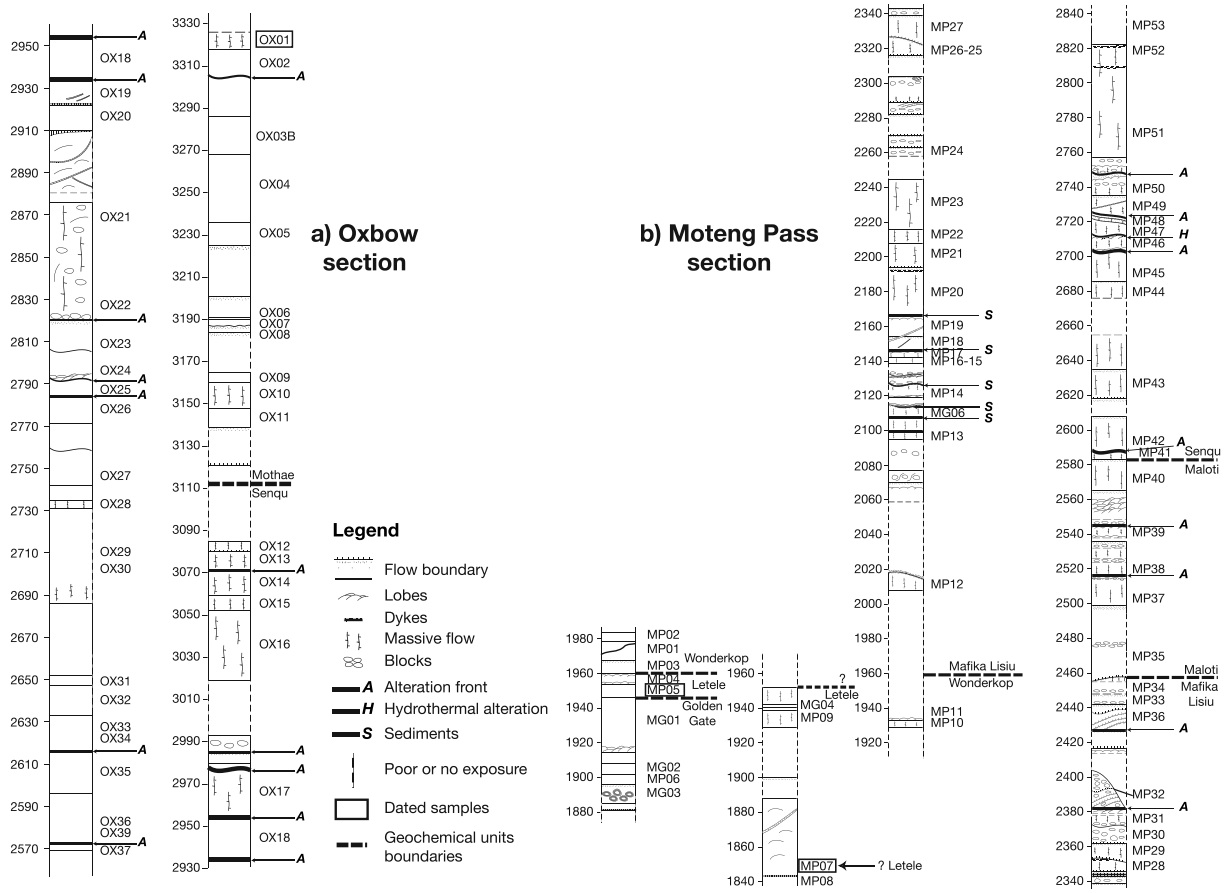

Figure 4. Stratigraphic logs of the (a) Oxbow and (b) Moteng Pass sections, with locations of paleomagnetic sites shown.

attention has been focused on the remarkably detailed record of the single reversal recorded in the Drakensberg group and identified by *Van Zijl et al.* [1962a, 1962b] 50 years ago. A detailed study of the reversal has been published by *Moulin et al.* [2012].

2.4. The Oxbow and Moteng Pass Sections

Our paleomagnetic and geochronologic (K-Ar and Ar-Ar) investigations of the Moteng Pass and Oxbow sections further north in Lesotho, where the Karoo lavas are the thickest (almost 1500 m) (Figure 1b), form the second phase of our research and are at the core of the present paper. We have sampled lava flows in these two new sections, near Oxbow (~760 m thick) and Moteng Pass (~1000 m thick) (Figures 1b and 3). The two sections overlap over ~290 m, yielding a 1500 m thick composite section, one of the thickest in the Drakensberg group, between altitudes 1850 and 3350 m (Figures 3 and 4). Our sampling strategy for paleomagnetic study has been based on logging the whole sections (Figures 4a and 4b). Careful volcanostratigraphic analysis included determination of the upper and lower boundaries of each flow, using characteristic volcanic features [see *Moulin et al.*, 2011].

We have identified lava flows based on the occurrence of pipe vesicles in what is interpreted as the basal layer of an upper lava unit, overlying vesicles in the surface crust of a lower lava unit. Flow thickness varies mostly from ~0.1 to ~20 m but can reach 60 m (e.g., a lava flow close to 2850 m along the Oxbow section —sites OX21 and OX22) (Figures 4a and 4b). Successive lava flows are occasionally separated by a weathered horizon and/or a sedimentary layer (Figures 4a and 4b). Five indurated sedimentary layers, 1 to 2 m thick, occur in the lower part of the Moteng Pass section (between 2100 and 2180 m elevation) (Figure 4b). These interbedded layers, which consist of detrital sediments with features similar to those found along the Naude's Nek section [*Moulin et al.*, 2011], are related to the Clarens Formation (the last sedimentary unit

of the Karoo Supergroup) [*Johnson et al*., 1996]. As is the case in the Naude's Nek section, there is no sediment layer in the upper part of the volcanic sequence [see *Moulin et al*., 2011, 2012, for more details]. About 20 weathered horizons and one hydrothermally altered lava contact have been observed within the two sections (Figures 4a and 4b). The reddish interflow layers consist essentially of basaltic saprolites (restricted alteration of the upper flow surface) mixed with colluvial deposits. From the base toward the upper part of the section, occurrence of detrital quartz decreases in the red colluvial paleosol interflow layers. Above 2930 m, the red interflows do not contain detrital quartz. The three red interflows above that altitude consist of a 10 to 30 cm thick red silty/clayey horizon (smectite-hematite) overlying the saprolite, corresponding to more mature paleosols. These layers are also affected by K-metasomatism. The undulating contacts suggest emplacement between frontal lobes that are more easily altered. The limited extent of interflow layers suggests arid climatic conditions that would have prevented extensive weathering.

We have sampled most of the flows for paleomagnetic analysis and selected the less weathered ones (from the bottom and the top of the composite sequence) for geochronologic analysis (Figures 3 and 4). Among the 97 paleomagnetic sites (generally labeled MP*n* or MG*n* for the Moteng Pass section and OX*n* for the Oxbow section), two were sampled in dykes (MP08 and DY01) (Figures 3 and 4). Ten samples were selected for dating along the two sections, one (OXMQ) coming from a basal lava flow slightly west of the Moteng Pass section (Figure 3).

Six geochemical units are encountered within the Moteng Pass section [*Marsh et al*., 1997]: the Golden Gate, Letele and Wonderkop units (within the Barkly East Formation) and the Mafika Lisiu, Maloti, and Senqu units (within the Lesotho Formation). The first outcropping lava flow (MP07) belongs to an undetermined geochemical unit with a composition close to the Letele unit (Figure 4b). The Oxbow section shows the two uppermost geochemical units of the Drakensberg group [*Marsh et al*., 1997]: the Senqu and Mothae units (within the Lesotho Formation) (Figure 4a).

3. Paleomagnetism

3.1. Procedure

We sampled at least eight cores for each paleomagnetic site (lava flow). Core orientation was measured using both magnetic and sun compasses. The positions of sites were determined using GPS (Figures 3 and 4). Laboratory techniques and data processing were identical to those performed in the study of the Naude's Nek section [*Moulin et al*., 2011]. We measured the magnetization of samples with a JR-5 spinner magnetometer in the shielded room of the paleomagnetic laboratory at the Institut de Physique du Globe de Paris. Comparison of stepwise thermal (13 to 15 steps up to 640°C in a nearly zero field laboratory-built furnace) and alternating field (11 steps up to 100 mT with an Agico LDA-3 demagnetizer) demagnetizations for pilot samples of the Oxbow section showed in most cases that thermal demagnetization was the more efficient method to isolate the characteristic remanent magnetization (ChRM). Remaining samples of the Oxbow section and all samples of the Moteng Pass section were therefore thermally demagnetized with about 7–12 demagnetization steps up to 640°C. To detect potential changes in magnetic mineralogy during thermal demagnetization, magnetic susceptibility was monitored after each heating step using a Kappabridge KLY-2 instrument. Demagnetization results were plotted on both orthogonal vector endpoint diagrams [*Zijderveld*, 1967] and in equal-area projection. Data processing used the PaleoMac software [*Cogné*, 2003]. Magnetization components were determined by principal component analysis [*Kirschvink*, 1980] or great circles [*McFadden and McElhinny*, 1988]. The majority of samples show either a well-defined ChRM with a single magnetization component (Figure 5, e.g., OX22-1B) or two components with the lower unblocking temperature component (LTC) typically below 300°C (Figure 5, e.g., MP24-6A).

A second more complex type of behavior involved two to three magnetization components. Although the destruction of the secondary components begins at temperatures above 300°C, it is almost always possible to isolate the ChRM above 460°C, up to 570°C or 640°C (Figure 5, e.g., MP13-5B). For a few specimens, the high-temperature component (HTC) could not be easily isolated from the LTC. Thus, the HTC had to be determined using the great circle method (Figure 5, e.g., OX34-5B). Complete demagnetization is generally reached between 570°C and 600°C (Figure 5, e.g., OX22-1B), though some samples are fully demagnetized only at higher temperatures, up to 640°C (Figure 5, e.g., MP24-6A, OX34-5B, and MP13-5B). Unblocking temperatures suggest that magnetization is mainly carried by some form of magnetite, in some cases with

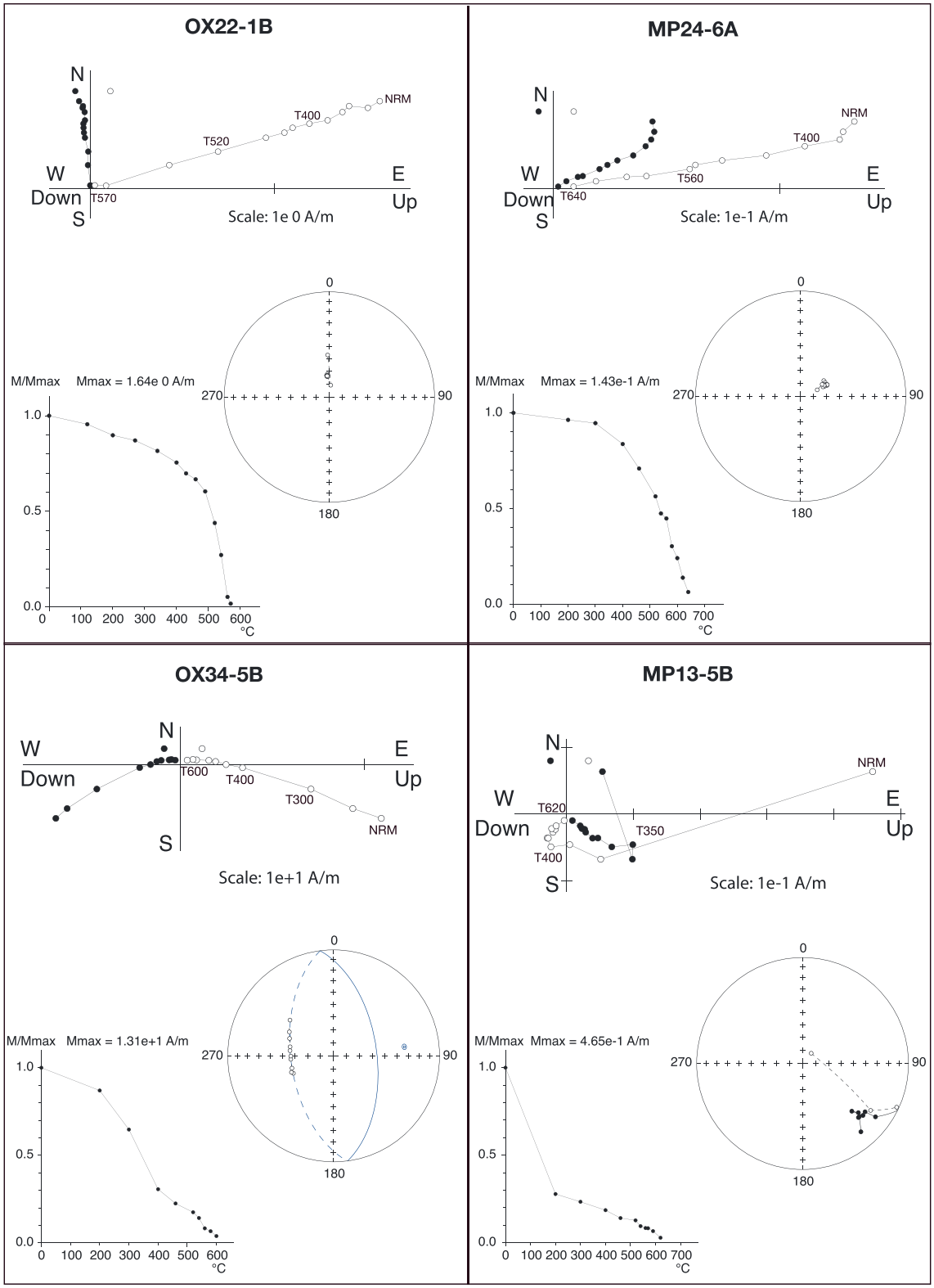

Figure 5. Four representative examples of thermal demagnetization from samples in the Oxbow (OX) and Moteng Pass (MP) sections. Orthogonal projections with several temperature steps indicated (NRM = natural remanent magnetization), equal-area projections, and thermal demagnetization diagrams are shown.

secondary hematite, possibly with some amount of titanium involved. A second mineral phase with a lower unblocking temperature (~400°C) corresponding to titanomagnetite has been detected in some samples (Figure 5, e.g., OX34-5B). Note that a few samples appear to contain a mineralogical phase with very low unblocking temperature (~100°C/200°C) (Figure 5, e.g., MP13-5B) that is difficult to identify based only on the demagnetization experiments.

3.2. Results

3.2.1. Site Mean Directions From Individual Sections

Site mean directions (based on five to nine core results) were calculated using either *Fisher* [1953] statistics for directions only or *McFadden and McElhinny* [1988] when both directional data and remagnetization circles had to be combined. Only two sites (OX03B and MP07) out of 96 display inconsistent magnetic directions (likely lightning induced). Two other sites (MP11 and MP12) sampled in the lower part of the Moteng Pass section (Figure 4b) raise problems: they display two directions of magnetization, a secondary component with normal polarity and a (reversed or transitional) characteristic component. Due to the small number and poor quality of characteristic directions used to calculate the mean magnetic directions of these two sites, they will not be used in the following.

Site mean directions are listed in Table 1 and illustrated on an equal-area projection (Figure 6a). In agreement with all previous paleomagnetic analyses of the Drakensberg group [*van Zijl et al*., 1962a, 1962b; *Kosterov and Perrin*, 1996; *Hargraves et al*., 1997; *Prévot et al*., 2003; *Moulin et al*., 2011, 2012], a single reversal is found within the two sections. The lower 12 sites (~90 m thick) of the Moteng Pass section have recorded a reversed polarity. We were not able to determine whether the two sites located just above (MP11 and MP12) have recorded the field in reversed polarity or during the reversal. However, site MP11 is located in the Wonderkop chemical unit, just below the Mafika Lisiu unit in which the magnetic reversal seems to have been systematically recorded. Site MP12 is in the Mafika Lisiu unit. Despite the lower-quality results, we can propose that the onset of the reversal occurred between sites MP11 and MP13. The following 13 sites (~170 m thick) are clearly transitional whereas the upper 29 sites (~520 m thick) have recorded a normal polarity. All lava flows of the Oxbow section (37 sites; ~760 m thick), which form the upper part of the Drakensberg volcanic sequence, have normal polarity.

3.2.2. Directional Groups and Construction of the Composite Oxbow-Moteng Pass Section

We have already identified successions of lava flows that display quasi-identical magnetic directions in the Naude's Nek section [*Moulin et al*., 2011]; they are called directional groups or pulses, depending on whether a paleomagnetic or volcanologic interpretation is selected. DGs are interpreted as an indication that eruptions lasted too little time to have recorded geomagnetic secular variation; hence, they are interpreted as single eruptive events. The concept of DGs has by now been extensively used in studies of LIP volcanism for the Columbia River basalts [*Mankinen et al*., 1985; *Jarboe et al*., 2008], North Atlantic igneous province [*Riisager et al*., 2002, 2003], Central Atlantic Magmatic Province [*Knight et al*., 2004], Siberian LIP [*Heunemann et al*., 2004; *Pavlov et al*., 2015], Deccan LIP [*Chenet et al*., 2008, 2009], and Karoo LIP itself [*Kosterov and Perrin*, 1996; *Prévot et al*., 2003; *Moulin et al*., 2011].

DGs are also present in the Oxbow and Moteng Pass sections (Figure 6b). The criteria used to define them are the same as for the Naude's Nek section [*Moulin et al*., 2011]. A directional group is inferred if the distances between the mean magnetic directions of the DG on one hand and each site mean direction on the other hand are lower than a threshold value defined as the square root of the sum of the squares of the 95% confidence cones of the directional group and respective paleomagnetic sites. Six paleomagnetic sites (OX04 and OX09 for the Oxbow section and MP14, MG06, MP08, and MP02 for the Moteng Pass section) that have a confidence cone α_{95} larger than 10° have been excluded from the analysis (Table 1).

The two sections studied in this paper have been divided into a succession of lava sets with similar magnetic directions and individual lava flows with magnetic directions that could not be merged with either underlying or overlying flows (see Figure 6b for an example). The lower part of the Moteng Pass section (~140 m thick) is a composite, constructed from geographically proximal locations (Figure 4b): three DGs (DG-OM1, DG-OM2, and DG-OM3) have been identified in the three small subsections at the base of the Moteng Pass section (Figure 7, bottom left). The Oxbow and Moteng Pass sections overlap over ~290 m (Figure 7). A comparison of the magnetic directions between the upper part of the Moteng Pass section and the lower part of the Oxbow section allows us to correlate them beyond doubt and to obtain a complete magnetic

Table 1. Site Mean Magnetic Directions of the Oxbow and Moteng Pass Sections[a]

Site	Directional Group or Single Flow	Elevation (m)	Slat (deg)	Slon (deg)	*n*/*N*	Dg (deg)	Ig (deg)	*K*	α_{95} (deg)
			Oxbow Section						
OX01	OM37	3320	−28.8105	28.7213	7/8	327.7	−38.4	74.6	7.0
OX02	OM36	3306	−28.8090	28.7193	6/8	336.6	−49.6	94.7	6.9
OX04		3237	−28.8157	28.7199	6/8	339.8	−40.8	49.5	10.0
OX05	OM35	3226	−28.8153	28.7182	7/8	332.9	−54.7	97.4	6.2
OX06	DG-OM34	3190	−28.8132	28.7156	8/8	332.7	−68.4	671.9	2.1
OX07	DG-OM34	3188	−28.8129	28.7151	8/8	334.2	−72.9	62.7	7.1
OX08	DG-OM34	3184	−28.8126	28.7149	8/8	335.4	−73.7	294.3	3.2
OX09		3163	−28.8113	28.7127	5/7	325.3	−82.5	39.7	13.2
OX10	OM33	3149	−28.8108	28.7119	8/8	312.0	−67.1	243.7	3.6
OX11	OM32	3140	−28.8100	28.7108	8/8	317.9	−62.2	310.9	3.1
OX12	DG-OM31	3081	−28.8079	28.7053	8/8	328.2	−54.1	972.8	1.8
OX13	DG-OM31	3072	−28.8079	28.7045	8/8	327.8	−55.7	459.6	2.6
OX14	DG-OM31	3060	−28.8076	28.7035	8/8	331.2	−54.9	210.1	3.9
OX15	DG-OM31	3053	−28.8075	28.7028	8/8	327.6	−54.4	453.4	2.6
OX16	DG-OM31	3020	−28.8067	28.6998	8/8	325.9	−53.0	702.7	2.1
OX17	DG-OM30	2969	−28.8042	28.6949	6/6	306.3	−53.2	1234.9	1.9
OX18	DG-OM30	2950	−28.8034	28.6938	6/7	309.2	−54.1	405.5	3.3
OX19	DG-OM29	2929	−28.8022	28.6922	8/8	336.8	−53.5	230.1	3.7
OX20	DG-OM29	2911	−28.8004	28.6905	8/8	338.9	−56.1	124.8	5.0
OX21	DG-OM28	2848	−28.7950	28.6867	8/8	343.5	−62.0	304.6	3.2
OX22	DG-OM28	2821	−28.7922	28.6836	8/8	347.1	−64.4	156.4	4.4
OX23	DG-OM28	2807	−28.7913	28.6833	6/6	341.6	−62.9	665.7	2.6
OX24	DG-OM26	2793	−28.7887	28.6824	9/10	329.3	−51.5	213.6	3.5
OX25	DG-OM26	2785	−28.7869	28.6817	8/8	325.2	−50.1	520.1	2.4
OX26	DG-OM26	2780	−28.7864	28.6813	8/8	334.2	−53.3	789.3	2.0
OX27	DG-OM25	2743	−28.7822	28.6766	8/8	324.2	−67.0	218.1	3.8
OX28	DG-OM25	2734	−28.7767	28.6736	8/8	330.7	−69.1	362.8	2.9
OX29	DG-OM25	2700	−28.7728	28.6690	6/6	320.8	−70.1	212.3	4.6
OX30	DG-OM23	2690	−28.7723	28.6680	9/10	325.2	−62.7	212.4	3.5
OX31	DG-OM23	2650	−28.7700	28.6655	8/8	329.1	−60.8	240.0	3.6
OX32	DG-OM22	2635	−28.7671	28.6605	8/8	329.1	−34.5	147.4	4.6
OX33	DG-OM22	2625	−28.7663	28.6595	5/8	333.3	−35.1	187.6	5.6
OX34	DG-OM22	2617	−28.7654	28.6574	8/8	328.3	−34.3	214.6	3.8
OX35	DG-OM22	2597	−28.7642	28.6540	8/8	327.3	−37.4	309.1	3.2
OX36	DG-OM21	2575	−28.7636	28.6520	8/8	310.5	−46.8	111.3	5.3
OX37	DG-OM19	2570	−28.7632	28.6505	8/8	343.2	−57.7	161.9	4.4
OX39	OM20	2574	−28.7692	28.6414	8/8	312.8	−57.3	297.0	3.2
			Moteng Pass Section						
MP53	OM27	2823	−28.7555	28.6012	7/8	318.0	−22.3	44.2	9.4
MP52	DG-OM26	2810	−28.7556	28.5992	8/8	331.6	−53.7	261.5	3.4
MP51	DG-OM26	2770	−28.7554	28.5965	8/8	327.5	−52.7	105.6	5.4
MP50	DG-OM25	2736	−28.7565	28.5942	8/8	334.1	−70.3	161.9	4.5
MP49	DG-OM25	2725	−28.7563	28.5933	8/8	333.8	−73.3	228.0	3.7
MP48	DG-OM25	2721	−28.7557	28.5925	8/8	322.6	−70.9	880.0	1.9
MP47	DG-OM25	2713	−28.7550	28.5925	8/8	336.4	−68.5	141.2	4.7
MP46	DG-OM25	2708	−28.7542	28.5924	8/8	331.3	−66.8	317.1	3.1
MP45	DG-OM24	2687	−28.7525	28.5918	8/8	333.3	−55.2	257.1	3.5
MP44	DG-OM24	2678	−28.7530	28.5916	8/8	331.5	−56.3	233.9	3.6
MP43	DG-OM22	2628	−28.7548	28.5902	8/8	334.8	−33.0	178.1	4.2
MP42	DG-OM22	2594	−28.7548	28.5886	8/8	329.8	−34.5	148.0	4.6
MP41	DG-OM22	2588	−28.7533	28.5875	8/8	332.5	−33.9	600.0	2.3
MP40	DG-OM21	2569	−28.7537	28.5873	8/8	315.7	−50.6	197.8	3.9
MP39	DG-OM19	2542	−28.7556	28.5882	8/8	337.0	−55.6	104.0	5.5
MP38	DG-OM18	2520	−28.7563	28.5882	8/8	343.4	−47.9	398.8	2.8
MP37	DG-OM18	2502	−28.7564	28.5874	8/8	339.8	−49.2	297.5	3.2
MP35	OM17	2469	−28.7576	28.5869	7/8	329.8	−60.5	231.5	4.0
MP34	OM16	2450	−28.7583	28.5871	8/8	344.2	−56.3	126.4	4.9
MP33	DG-OM15	2445	−28.7594	28.5872	8/8	329.8	−52.3	197.8	3.9
MP36	DG-OM15	2434	−28.7598	28.5875	8/8	328.6	−51.9	335.5	3.0
MP32	DG-OM14	2382	−28.7633	28.5843	8/8	338.9	−51.1	362.7	2.9

Table 1. (continued)

Site	Directional Group or Single Flow	Elevation (m)	Slat (deg)	Slon (deg)	*n*/*N*	Dg (deg)	Ig (deg)	*K*	α_{95} (deg)
MP31	DG-OM14	2375	−28.7648	28.5832	6/8	341.4	−53.9	200.7	4.7
MP30	DG-OM14	2371	−28.7642	28.5823	7/8	346.6	−48.4	216.6	4.1
MP29	DG-OM14	2355	−28.7640	28.5813	8/8	350.4	−53.4	1152.8	1.6
MP28	DG-OM14	2347	−28.7641	28.5805	8/8	348.5	−53.5	483.4	2.5
MP27	DG-OM13	2330	−28.7638	28.5806	8/8	354.5	−71.8	276.4	3.3
MP26	DG-OM13	2320	−28.7637	28.5808	7/8	347.3	−75.0	51.3	8.5
MP25	OM12	2318	−28.7636	28.5816	7/8	4.2	−60.9	66.3	7.5
MP24	OM11	2247	−28.7644	28.5768	8/8	68.2	−68.3	189.5	4.0
MP23	OM10	2226	−28.7647	28.5749	7/8	86.2	−70.9	274.2	3.7
MP22	OM9	2212	−28.7647	28.5741	8/8	64.3	−69.0	612.7	2.2
MP21	DG-OM8	2197	−28.7647	28.5727	8/8	94.9	−72.8	234.3	3.6
MP20	DG-OM8	2174	−28.7653	28.5701	6/8	97.9	−76.6	83.3	7.4
MP19	OM7	2158	−28.7662	28.5694	7/8	38.8	−63.1	104.0	5.9
MP18	OM6	2150	−28.7657	28.5687	6/8	6.4	−40.0	89.4	7.1
MP17	DG-OM5	2143	−28.7656	28.5677	6/7	114.7	17.2	77.4	7.8
MP16	DG-OM5	2141	−28.7657	28.5668	8/8	121.5	19.2	88.6	5.9
MP15	DG-OM5	2140	−28.7655	28.5659	8/8	116.1	25.0	50.3	8.2
MP14		2121	−28.7641	28.5617	7/8	138.4	18.4	32.3	10.9
MP13	OM4	2096	−28.7615	28.5534	7/8	135.7	23.2	198.3	4.3
MG06		2111	−28.7620	28.5531	6/8	120.2	16.1	23.8	15.0
MP10	DG-OM3	1930	−28.7588	28.5312	8/8	169.5	71.5	79.0	6.3
MG04	DG-OM2	1944	−28.7645	28.5105	8/8	182.0	52.3	819.7	1.9
MP09	DG-OM2	1931	−28.7645	28.5105	8/8	182.2	54.3	223.6	3.7
MP08		1843	−28.7687	28.5067	8/8	349.7	−45.0	233.8	3.6
MG03	DG-OM1	1888	−28.7651	28.5034	8/8	155.8	66.5	498.8	2.5
MP06	DG-OM1	1895	−28.7641	28.4988	8/8	159.2	63.5	278.3	3.3
MG02	DG-OM1	1899	−28.7633	28.4991	6/8	162.8	64.2	103.4	6.6
MG01	DG-OM1	1930	−28.7616	28.4943	8/8	156.9	64.2	305.0	3.2
MP05	DG-OM2	1949	−28.7624	28.4931	8/8	180.6	51.5	532.7	2.4
MP04	DG-OM3	1959	−28.7635	28.4908	6/6	158.4	70.8	110.8	6.4
MP03	DG-OM3	1962	−28.7635	28.4908	7/7	158.9	74.5	994.5	1.9
MP02		1979	−28.7601	28.4842	8/8	147.9	73.1	40.4	11.1
MP01	DG-OM3	1968	−28.7600	28.4836	8/8	150.6	75.0	226.6	3.7

[a]Site mean magnetic directions are numbered from 1 to 37 (DG-OM*x* when the site belongs to a directional group or OM*x* for a single flow) (see text and Table 2); elevation (m), latitude Slat (deg), and longitude Slon (deg) are the coordinates of paleomagnetic sites; *n*/*N*: *N* is the number of samples measured and *n* the number used in calculating the mean direction; Dg and Ig are the site mean declination and inclination of the characteristic remanent magnetization; *K* is the Fisher precision parameter; α_{95} is the 95% confidence interval.

stratigraphy of the northern part of the Drakensberg group. Five directional groups (DG-OM19, DG-OM21, DG-OM22, DG-OM25, and DG-OM26) are common to both sections (Figure 7). Lava flows belonging to the same DGs have similar elevations in the two sections. This implies a spatially homogeneous eruption of the flows over a distance of at least 20 km.

Mean magnetic directions of DGs were obtained by averaging magnetic directions of samples rather than those of sites (Table 2), a difference with respect to what was done in the Naude's Nek section [*Moulin et al.*, 2011]. This allows direct comparison between our results and those obtained in *Kosterov and Perrin* [1996] and *Prévot et al.* [2003]. Mean magnetic directions obtained by the two methods are very close: on average, differences in declination and inclination are less than 0.1°. However, the 95% confidence interval obtained using magnetic directions of all samples is significantly lower (by a factor of 2.2 on average) than when using site means. A total of 37 distinct magnetic directions, comprising 21 directional groups and 16 individual lava flows, were identified for the composite Oxbow-Moteng Pass section (Table 2, Figures 6c and 7). The correlation of magnetic directions between the two sections yields the thickest volcanic sequence of the Drakensberg group (~1500 m).

3.2.3. Reversal Test and Magnetic Poles

In order to avoid an overrepresentation of site mean magnetic directions belonging to DGs, reversal tests and mean magnetic directions were calculated using distinct magnetic directions of DGs and individual lava flows. The two mean directions for reversed and normal polarities of the Oxbow-Moteng Pass section pass

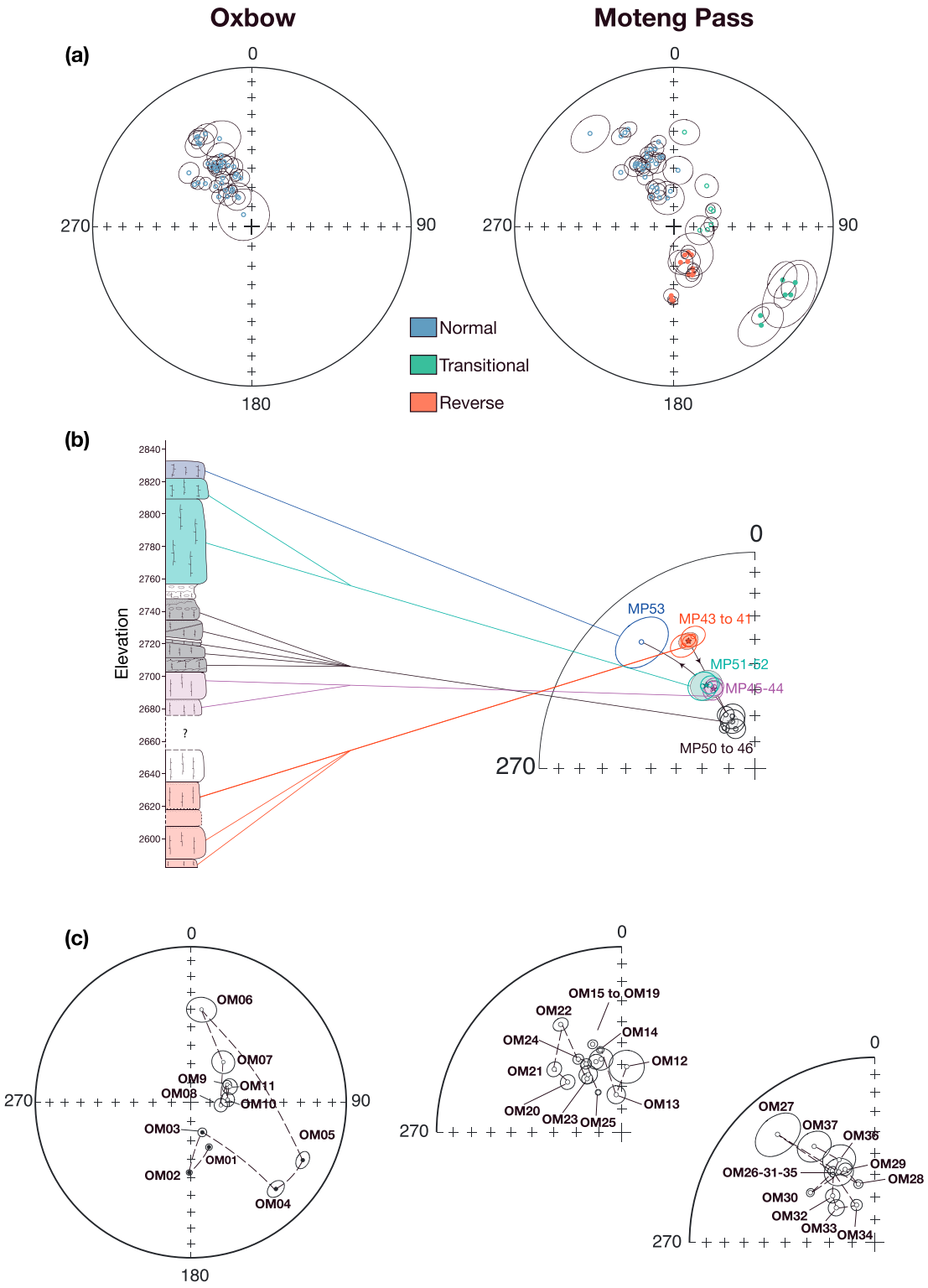

Figure 6. (a) Equal-area projection of all site mean directions and their 95% confidence intervals. Normal polarity: blue circles; reverse polarity: orange circles; transitional polarity: green circles. Open symbols: upper hemisphere; closed symbols: lower hemisphere. (b) Example of directional groups and individual lava flows defined from mean magnetic directions of lava flows in the upper part of the Moteng Pass section. (c) Equal-area projections of the 37 distinct magnetic directions (directional groups and individual lava flows) identified along the Oxbow-Moteng Pass composite section (see text and Table 2 for link between magnetic direction numbers and paleomagnetic sites; directions are connected in stratigraphic order from bottom to top of the section and shown as three separate, successive diagrams in order to avoid overlap).

Table 2. Distinct Magnetic Directions Numbered From 1 to 37 in Stratigraphic Order[a]

Directional Group or Single Flow	Site(s)	*N*	Dg (deg)	Ig (deg)	*K*	α_{95} (deg)
OM37	OX01	7	327.7	−38.4	74.6	7.0
OM36	OX02	6	336.6	−49.6	94.7	6.9
OM35	OX05	7	332.9	−54.7	97.4	6.2
DG-OM34	OX06 to OX08	24	334.0	−71.6	142.2	2.5
OM33	OX10	8	312.0	−67.1	243.7	3.6
OM32	OX11	8	317.9	−62.2	310.9	3.1
DG-OM31	OX12 to OX16	40	328.1	−54.4	427.6	1.1
DG-OM30	OX17, OX18	12	307.8	−53.7	606.2	1.8
DG-OM29	OX19, OX20	16	337.8	−54.8	163.7	2.9
DG-OM28	OX21 to OX23	22	344.3	−63.1	254.9	1.9
OM27	MP53	7	318.0	−22.3	44.2	9.4
DG-OM26	MP51, MP52; OX24 to OX26	41	329.3	−52.8	131.5	2.0
DG-OM25	MP50 to MP46; OX27 to OX29	62	329.4	−69.6	204.3	1.3
DG-OM24	MP45, MP44	16	332.4	−55.8	256.4	2.3
DG-OM23	OX30, OX31	17	327.1	−61.8	223.9	2.4
DG-OM22	MP41 to MP43; OX32 to OX35	53	330.4	−33.6	41.4	3.1
DG-OM21	MP40; OX36	16	313.0	−48.7	131.8	3.2
OM20	OX39	8	312.8	−57.3	297.0	3.2
DG-OM19	MP39; OX37	16	339.8	−56.7	124.5	3.3
DG-OM18	MP37, MP38	16	341.6	−48.6	329.0	2.0
OM17	MP35	7	329.8	−60.5	231.5	4.0
OM16	MP34	8	344.2	−56.3	126.4	4.9
DG-OM15	MP36, MP33	16	329.2	−52.1	264.4	2.3
DG-OM14	MP28 to MP32	37	345.3	−52.1	230.1	1.6
DG-OM13	MP26, MP27	15	351.5	−73.3	93.1	4.0
OM12	MP25	7	4.2	−60.9	66.3	7.5
OM11	MP24	8	68.2	−68.3	189.5	4.0
OM10	MP23	7	86.2	−70.9	274.2	3.7
OM9	MP22	8	64.3	−69.0	612.7	2.2
DG-OM8	MP20, MP21	14	96.0	−74.5	132.9	3.5
OM7	MP19	7	38.8	−63.1	104.0	5.9
OM6	MP18	6	6.4	−40.0	89.4	7.1
DG-OM5	MP15 to MP17	22	117.5	20.4	64.0	3.9
OM4	MP13	7	135.7	23.2	198.3	4.3
DG-OM3	MP01, MP03, MP04; MP10	29	159.9	73.2	137.9	2.3
DG-OM2	MP05, MP09; MG04	24	181.6	52.7	392.3	1.5
DG-OM1	MG01 to MG03; MP06	30	158.5	64.6	237.8	1.7

[a]DG-OMx is for a directional group, and OM*x* is only for a single flow (see text). *N* represents the number of paleomagnetic samples defining the cooling unit. Other column headings are the same as those in Table 1.

a class C reversal test [*McFadden and McElhinny*, 1990] (Figure 8a). The level C can be explained by the small number of data with reversed polarity. For the Naude's Nek section, we showed that the reversal test failed, although the two 95% confidence intervals did intersect [*Moulin et al*., 2011]. We have now been able to confirm that the lava flows from the Moshesh's Ford unit in the lower part of the Naude's Nek section (directional groups 1 to 4) are significantly older than those from the upper part of the section (see *Moulin et al*. [2011] and discussion section in this paper). The Moshesh's Ford unit was therefore removed from the reversal test and, as a result, the Naude's Nek section now passes the level C (Figure 8b). As for the Oxbow-Moteng Pass section, the number of directions with reversed polarity is insufficient (only two) to average out secular variation and the corresponding mean magnetic direction has a large uncertainty. Combining data from the two sections (Naude's Nek and Oxbow-Moteng Pass), the reversal test is again positive (class C) (Figure 8c). Although the 95% reverse polarity confidence interval remains very large (14.6°), the two directions are only 3.1° apart. There is little doubt that the whole set of characteristic directions determined for the Karoo sections does represent the paleofield accurately.

The mean direction based on the mean magnetic directions of all directional groups and individual lava flows of the Oxbow-Moteng Pass section, excluding transitional directions, is $D = 332.2°$, $I = -56.7°$ ($N = 29$, $\alpha_{95} = 4.5°$). The virtual geomagnetic pole (VGP) derived from that mean direction lies at lat = 65.3°N, long = 267.9°E ($A_{95} = 5.2°$) (Figure 8d and Table 3). The mean direction based on 15 distinct magnetic

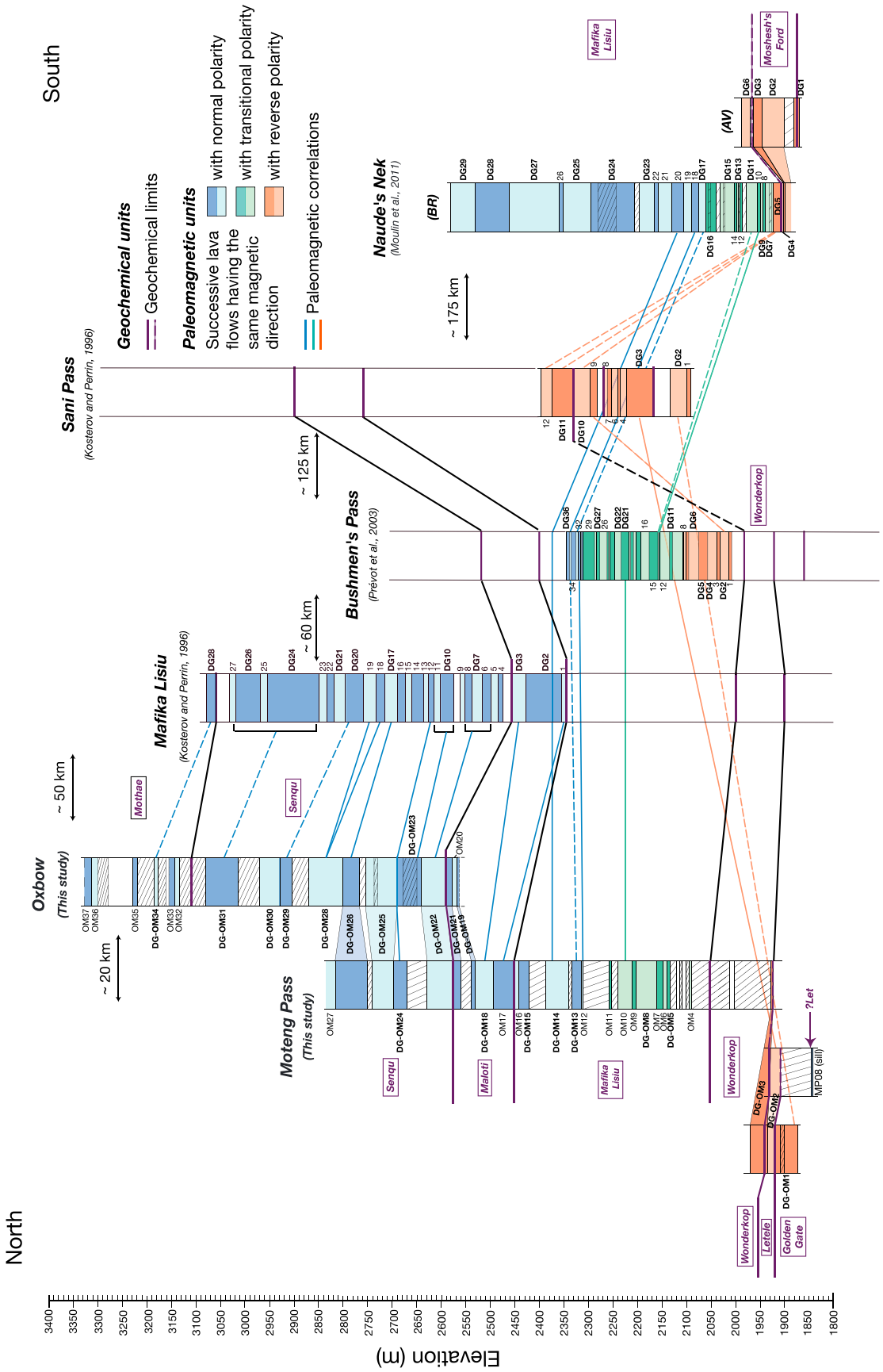

Figure 7. Synthesis of volcanic stratigraphy along five sections (arranged from north to south; see Figure 1b for locations): the composite section sampled during this study (Oxbow-Moteng Pass) and four other sections from previous studies. Color codes correspond to the different directional groups (DGx) or individual lava flows (*x*) in reverse (orange), transitional (green), or normal (blue) polarities. Magnetic correlations between sections are shown by colored full or dashed lines (connections for which we are less certain). The stratigraphic locations of geochemical boundaries within the Oxbow-Moteng Pass section and within the BR traverse of the Naude's Nek sections are shown as connected thicker black lines, based on geochemical analyses [*Marsh et al.*, 2011; unpublished data]. Within the AV traverse of the Naude's Nek section, the boundaries are estimated according to paleomagnetic correlations between the AV and BR traverses [*Moulin et al.*, 2011].

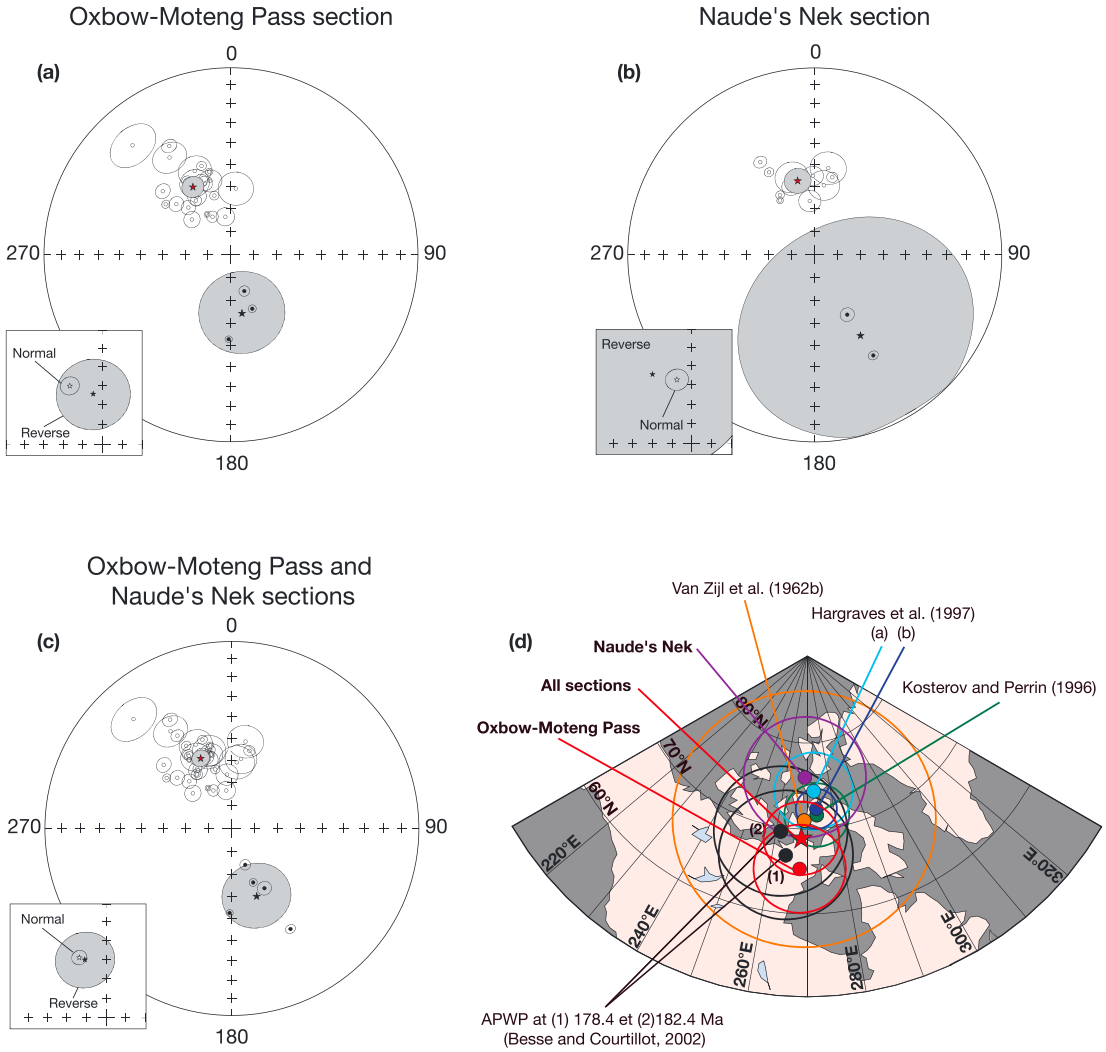

Figure 8. Equal-area projections of mean magnetic directions obtained for reversed and normal polarities for (a) the Oxbow-Moteng Pass section, (b) the Naude's Nek section, and (c) both sections combined. Mean magnetic directions were calculated using distinct magnetic directions obtained for DGs and individual lava flows. Overall means for respectively normal and reversed polarities shown as insets. (d) Equal-area projection of virtual geomagnetic poles (VGPs) for the Drakensberg group with 95% confidence intervals projected on the northern hemisphere. The blue circle (labeled "a") corresponds to the mean VGP of *Hargraves et al.* [1997], recalculated (dark blue circle, labeled "b") by *Moulin et al.* [2011].

directions (DGs or individual lava flows of normal or reverse polarities, excluding the Moshesh's Ford unit) of the Naude's Nek section is $D = 344.3°$, $I = -55.6°$ ($N = 15$, $\alpha_{95} = 5.6°$). The mean paleomagnetic pole has coordinates at lat = 76.0°N, long = 268.8°E ($A_{95} = 7.0°$) (Figure 8d and Table 3). The overall mean direction obtained for distinct magnetic directions of the two sections (Naude's Nek and Oxbow-Moteng Pass) is $D = 336.4°$, $I = -56.5°$ ($N = 44$, $\alpha_{95} = 3.5°$), and the coordinates of the corresponding VGP are lat = 68.9°N, long = 268.1°E ($A_{95} = 4.3°$) (Figure 8d and Table 3). This corresponds to a paleolatitude of $-38.4° \pm 4.3°$. This pole is close to and consistent with previous determinations by *van Zijl et al.* [1962a, 1962b], *Kosterov and Perrin* [1996], and *Hargraves et al.* [1997] and to the pole that we have recalculated from the data of *Hargraves et al.* [1997] in our previous study [*Moulin et al.*, 2011] (Figure 8d and Table 3). Our pole agrees with the synthetic poles of *Besse and Courtillot* [2002] for Africa in the 175–185 Ma range (Figure 8d and Table 3).

4. Geochronology

K-Ar and $^{40}Ar/^{39}Ar$ dating were performed in the GEOPS laboratory at the University of Paris-Sud (Orsay, France). Decay constants and isotopic ratios of *Steiger and Jäger* [1977] were used. Thirteen lava flows were

Table 3. Drakensberg Group Virtual Geomagnetic Poles (VGPs)[a]

Sections	*N*	VGP Lat. (°N)	VGP Long. (°E)	K	A_{95}	References
Oxbow-Moteng Pass	29[b]	65.3	267.9	27.9	5.2	This study
Naude's Nek	15[b]	76.0	268.8	30.8	7.0	This study
Naude's Nek ; Oxbow-Moteng Pass	44[b]	68.9	268.1	26.5	4.3	This study
Sani Pass, Bushman's Pass	74[b]	71.0	269.0	104.0	15.0	*Van Zijl et al.* [1962a, 1962b]
Sani Pass, Nazareth, Rhodes, Mafika Lisiu	47[b]	71.6	273.5	33.0	3.7	*Kosterov and Perrin* [1996]
OXB, BTW, LTW, MPLPW, MKH, LTE, MLPE, KAT, SOM, SP, ON	11[c]	74.4	272.8	104.0	4.5	*Hargraves et al.* [1997]
OXB, BTW, LTW, MPLPW, MKH, LTE, MLPE, SOM, SP, ON	10[c]	72.3	273.5	427.4	2.3	*Moulin et al.* [2011, recalculated from data of *Hargraves et al.*, 1997]
APWP at 178.4 Ma	12	66.8	263.9	33.4	7.6	*Besse and Courtillot* [2002]
APWP at 182.4 Ma	9	69.5	261.4	46.5	7.6	*Besse and Courtillot* [2002]

[a]VGP Lat. and VGP Long. are the latitude and longitude of the VGP; *K* is the Fisher precision parameter; A_{95} is the 95% confidence interval.
[b]*N* is the number of distinct magnetic directions (DGs and individual lava flows, or equivalent).
[c]*N* is The number of section mean magnetic directions used in calculating VGPs.

sampled in the Oxbow-Moteng Pass section, evenly distributed throughout the section and as little weathered as possible. Most samples display the same texture and mineralogy as the basalts of the Naude's Nek section [*Moulin et al.*, 2011]. A careful petrographic study of thin sections allowed us to select four samples from the Oxbow-Moteng Pass section with optically unaltered plagioclase microcrystals for K-Ar dating. In order to test the K-Ar ages obtained for the Naude's Nek section [*Moulin et al.*, 2011] and for the Oxbow-Moteng Pass section (this study), we also performed $^{40}Ar/^{39}Ar$ analyses on four of our samples (two for each section). Unless specified otherwise, all K-Ar and $^{40}Ar/^{39}Ar$ uncertainties are quoted at the 1 sigma level.

4.1. Procedure

4.1.1. K-Ar Technique

As in *Moulin et al.* [2011], we have used the unspiked K-Ar dating based on the Cassignol-Gillot K-Ar technique, which is fully described in *Cassignol and Gillot* [1982] and *Gillot and Cornette* [1986]. Based on the microcrystal size distribution of plagioclase observed in each sample, crushing and sieving were performed in the 125–250 and 100–200 μm size ranges. In one sample (OX01, Table 4) that contained both plagioclase microcrystals and phenocrysts, heavy liquids were used first, to separate phenocrysts in the 250–500 μm size fraction. The crushed fractions were cleaned with deionized water and then placed in an ultrasonic bath for 15 min with a 5% nitric or acetic acid solution in order to remove possible traces of weathered material. Minerals were separated from the groundmass using heavy liquids and using a Frantz magnetic separator. Following dissolution of pure plagioclase crystals in a mixture of acids [see *Moulin et al.*, 2011], potassium was measured by atomic absorption spectrophotometry. Signal intensity was converted into K content using

Table 4. ^{40}K-^{40}Ar Ages of the Oxbow and Moteng Pass Section[a]

Sample	Elevation (m)	Phase	K%	% $^{40}Ar^*$	$^{40}Ar^*$ (at/g)	Age ± 1σ (Ma)	Mean Age ± 1σ (Ma)	Polarity
OX01	3320	m	0.357	90.8	7.0229E+13	179.1 ± 2.5	180.3 ± 2.6	N
				70.8	7.1280E+13	181.7 ± 2.6		
OX01	3320	p	0.127	80.4	2.4731E+13	177.4 ± 2.5	175.5 ± 2.5	N
				81.2	2.4164E+13	173.5 ± 2.5		
MP05-09	1949	m	0.184	89.7	3.5962E+13	178.0 ± 2.6	182.1 ± 2.6	R
				93.3	3.7435E+13	185.0 ± 2.7		
				86.0	3.7086E+13	183.3 ± 2.6		
OXMQ	1892	m	0.144	72.0	2.9076E+13	183.7 ± 2.6	182.8 ± 2.6	?
				57.6	2.8756E+13	181.7 ± 2.6		
MP07-09	1844	m	0.135	84.0	2.6859E+13	181.1 ± 2.6	181.4 ± 2.6	?
				80.3	2.6948E+13	181.7 ± 2.6		

[a]Samples are listed in stratigraphic order from the lowest (MP07-09, 1844 m) to uppermost (OX01, 3320 m). Phase: mineralogical phase analyzed (m: microlites, p: phenocrysts); K%: potassium concentration in percent; % $^{40}Ar^*$: concentration of radiogenic ^{40}Ar in percent; $^{40}Ar^*$ (at/g): number of atoms per gram of radiogenic ^{40}Ar; age in Ma with 1σ uncertainty; mean age in Ma (average of two or three specimens in same sample) with 1σ uncertainty and magnetic polarity of each sample.

a calibration curve obtained between 1 and 2 ppm K using a pure K standard solution. The MDO-G standard and the BCR-2 international geostandard were used to check this calibration [*Gillot et al*., 1992]. Argon was measured with a mass spectrometer similar to the one described in *Gillot and Cornette* [1986] after gas extraction and purification [see *Moulin et al*., 2011, for more details]. Prior to each analysis, an absolute calibration of the ^{40}Ar signal was performed with the measurement of a 0.1 cm^3 aliquot collected with an air pipette calibrated by repeated analyses of the interlaboratory standard GL-O with a recommended value of ^{40}Ar* of 6.679×10^{14} atom/g [*Odin et al*., 1982] and of the HD-B1 standard with a recommended value of 24.21 Ma [*Fuhrmann et al*., 1987; *Schwarz and Trieloff*, 2007]. This technique relies on a double isotopic comparison between the ^{40}Ar/^{36}Ar ratio of atmospheric argon and that of the sample. This direct comparison and the stable analytical conditions of the mass spectrometer require no assumption regarding the true value of the atmospheric ^{40}Ar/^{36}Ar ratio or mass discrimination correction, and there is no need for a ^{38}Ar spike in order to obtain precise measurements [*Gillot et al*., 2006]. Typical uncertainties of 1% are reached for the ^{40}Ar signal calibration and K content measurement. The uncertainty on the ^{40}Ar* determination, which is a function of the radiogenic content of the sample, is negligible in our case (these are "old" rocks containing between 56.3% and 93.3% of radiogenic ^{40}Ar; see Table 3). The detection limit of our mass spectrometer is 0.1% for the ^{40}Ar* signal [*Quidelleur et al*., 2001].

4.1.2. ^{40}Ar/^{39}Ar Technique

Samples NN45, NN57-m, MP05-09, and MP07-09 were irradiated for 60 h in the Cadmium-Lined In-Core Irradiation Tube position of the TRIGA reactor at the Radiation Center, Oregon State University (USA). The *J* factor was determined using the Fish Canyon Tuff sanidine (FCTs) standard with the recommended age of 28.201 Ma from *Kuiper et al*. [2008]. Aliquots of about 20 mg of FCTs were placed in vacuum-sealed quartz tubes between each sample, at about 8 mm intervals. Gas extraction from the flux monitors was performed with a Nd-YAG infrared laser, whereas samples were step-heated in a high-frequency furnace. The complete description of the multicollection mass spectrometer used in this study is given in *Coulié et al*. [2004]. Interfering reactions from K and Ca were accounted for using values of 6.0×10^{-4}, 1.2×10^{-2}, 7.2×10^{-4}, and 2.68×10^{-4}, respectively, for $(^{40}Ar/^{39}Ar)_K$, $(^{38}Ar/^{39}Ar)_K$, $(^{39}Ar/^{37}Ar)_{Ca}$, and $(^{36}Ar/^{37}Ar)_{Ca}$ [*Renne et al*., 1998]. Because measurements were performed with a multicollection instrument, plagioclase samples were measured about 7 months after irradiation, in order to allow for ^{37}Ar to decay significantly and hence to limit its influence on the small ^{36}Ar peak. Calculations of ages and uncertainties were performed following *McDougall and Harrison* [1999].

4.2. Results

4.2.1. K-Ar Ages

K-Ar ages obtained for the Oxbow-Moteng Pass section are listed in Table 4. K contents and Ar measurements were always at least duplicated for each sample. Mean ages and uncertainties have been calculated by weighting each duplicate by its radiogenic ^{40}Ar content. All duplicates used to determine mean ages give similar values at the 1σ level, except for MP05-09, which yields consistent ages at the 2σ level only (Table 4). For sample OX01, both plagioclase microcrystal and phenocryst fractions were analyzed. Although their mean ages are statistically similar at the 1σ level, the phenocrysts yield a K-Ar age younger than the microcrystals (Table 4). Since the K content of microcrystals is 3 times larger than that of phenocrysts and for consistency with other samples of the section presented in this study, we consider only the mean age obtained from the microcrystal phase for sample OX01. The four mean ages obtained along the Oxbow-Moteng Pass section display concordant values from 182.8 ± 2.6 Ma (OXMQ) to 180.3 ± 2.6 Ma (OX01) (Table 4) and are statistically undistinguishable at the 1σ level.

4.2.2. ^{40}Ar/^{39}Ar Ages

Four samples were analyzed for ^{40}Ar/^{39}Ar dating. Two of the four age spectra (MP05-09 and NN45) (Figure 9) display rather flat patterns, although the first 10–15% and the last 10–20% of ^{39}Ar released show slightly older apparent ages. The flat portions of spectra yield plateau ages of 181.0 ± 0.8 and 182.2 ± 0.9 Ma for MP05-09 and NN45, respectively. Both remaining samples, MP07-09 and NN57-m, display concordant step ages, with plateau ages of 180.1 ± 1.4 and 189.0 ± 0.9 Ma, respectively, although MP07-09 shows younger ages for the initial steps (the first 15% of the total ^{39}Ar yield) (Figure 9). The Ca/K mean ratio ranges from 20.9 to 64.7 (Figure 9 and Table S1 in the supporting information). Ca/K spectra slightly decrease and then increase toward the higher-temperature steps (Figure 9). This could be due to compositional zoning, but there is no systematic relationship with age patterns.

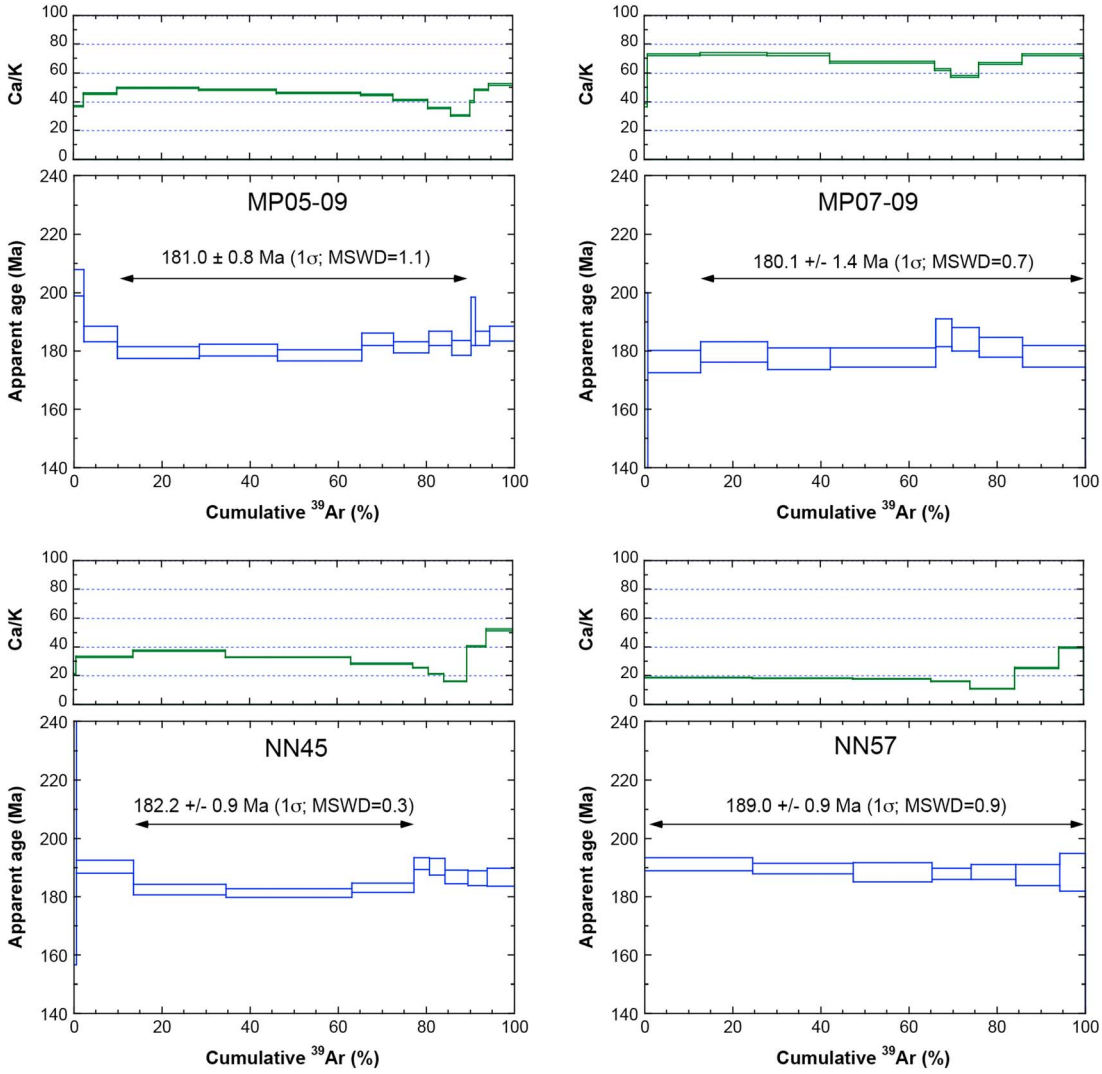

Figure 9. ^{40}Ar/^{39}Ar apparent age spectra and associated Ca/K ratios determined from Ar isotope data. Ages are based on decay constants of *Steiger and Jäger* [1977] and 28.201 Ma for the FCTs standard [*Kuiper et al.*, 2008]. The mean square of the weighted deviates is calculated for steps included in the plateau age.

Detailed ^{40}Ar/^{39}Ar results are shown in Table S1 and summarized in Table 5. We obtained four plateau ages (Figure 9 and Table 5) ranging from 189.0 ± 0.9 to 180.1 ± 1.4 Ma (1σ uncertainty). Three of them (MP05-09, MP07-09, and NN45), though spanning 2.1 Ma (between 180.1 and 182.2 Ma), have statistically similar ages at the 1σ level. On the other hand, the plateau age obtained for sample NN57-m appears to be older and is further discussed below.

4.2.3. Comparisons Between K-Ar and ^{40}Ar/^{39}Ar Ages

Four of the nine K-Ar ages obtained along the Naude's Nek section [*Moulin et al.*, 2011] and along the Oxbow-Moteng Pass section (this study) were also dated with the ^{40}Ar/^{39}Ar technique. A direct comparison between

Table 5. ^{40}Ar/^{39}Ar Ages of the Naude's Nek and Oxbow-Moteng Pass Sections and Comparison With K-Ar Ages[a]

Sample	Plateau Age (Ma)	1σ Uncertainty (Ma)	MSWD	% Gas	Total Gas Age (Ma)	K-Ar Age (Ma)
NN45	182.2	0.9	0.3	64	184.6 ± 2.9	179.0 ± 2.5
NN57	189.0	0.9	0.9	100	189.2 ± 3.3	184.8 ± 2.6
MP05-09	181.0	0.8	1.1	80	181.9 ± 2.9	182.1 ± 2.6
MP07-09	180.1	1.4	0.7	87	178.9 ± 4.2	181.4 ± 2.6

[a]Plateau ages (in Ma) are given with the 1σ uncertainty and calculated as the weighted mean of steps included in the plateau. The mean square of the weighted deviates (MSWD) is calculated for steps included in the plateau age.

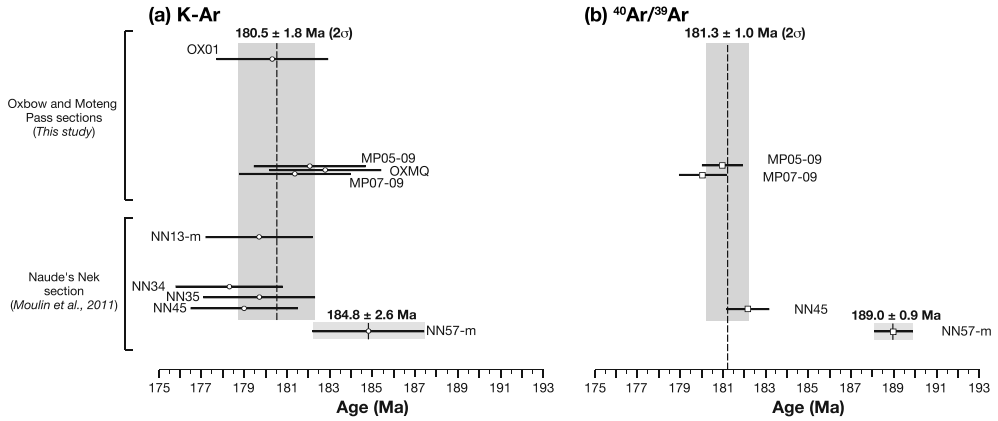

Figure 10. (a) Comparisons of the K-Ar ages (shown by circles) obtained for the Oxbow-Moteng Pass section (this study; see Table 4) and the Naude's Nek section [*Moulin et al*., 2011]. (b) $^{39}Ar/^{40}Ar$ plateau ages (shown by squares) obtained for the two sections (this study; see Table 5). Ages relative to FCTs at 28.201 Ma [*Kuiper et al*., 2008] and *Steiger and Jäger* [1977] decay constants. In each section, ages are plotted in stratigraphic order. The dashed vertical lines and shaded gray bands represent the mean ages and uncertainties (at the 2σ level) for each subset.

the ages obtained using both techniques is possible using the $^{40}Ar/^{39}Ar$ total gas ages and the K-Ar ages, which should be similar (Table 5). Three out of four samples (MP07-09, MP05-09, and NN57-m) yielded similar ages at the 1σ level (Table 5). Sample NN45 dated at 179.0 ± 2.5 Ma by the K-Ar technique gives a slightly older $^{40}Ar/^{39}Ar$ total gas age of 184.6 ± 2.9 Ma, with a difference at the edge of statistical significance at the 1σ level, but in agreement at the 2σ level. The higher value shown by the $^{40}Ar/^{39}Ar$ total gas technique can be explained by the older ages observed for the first two degassing steps. This could be due to ^{37}Ar recoil, which can be a concern for the initial degassing of Ca-rich plagioclase microcrystals [e.g., *Onstott et al*., 1995]. However, we note that $^{40}Ar/^{39}Ar$ plateau ages and K-Ar ages all agree at the 1σ level and therefore highlight the consistency of the two techniques for our samples, as previously observed for other volcanic LIP samples [*Coulié et al*., 2003; *Courtillot et al*., 2010; *Ricci et al*., 2013].

K-Ar results for NN45 and NN57-m samples are younger than $^{40}Ar/^{39}Ar$ total gas ages, whereas samples MP05-09 and MP07-09 show a slight tendency toward older values using the K-Ar technique. This observation indicates that there is no systematic error induced by the calibration of either the GL-O and HD-B1 standards used for K-Ar or the FCTs monitor used for $^{40}Ar/^{39}Ar$. Indeed, dating of the MMhb-1 standard provided K-Ar ages of 525 ± 2 Ma using the GL-O standard [*Fiet et al*., 2006] (with the same instrument and analytical conditions as used in the present study and in the work of *Moulin et al*. [2011]). This age is compatible with the recalculated value of 525.6 Ma from *Renne et al*. [1998], if the newly proposed age of 28.20 Ma is considered for FCTs [*Kuiper et al*., 2008].

5. An Attempt to Reconstruct the Eruptive History of the Drakensberg Group

5.1. Constraints From Geochronological Data

The four new K-Ar ages from the Oxbow-Moteng Pass section are consistent with the four uppermost samples of the Naude's Nek section at the 1σ level (*Moulin et al*. [2011] and Figure 10a) and altogether yield a $(1/\sigma^2)$ weighted mean age of 180.5 ± 1.8 Ma (2σ). The K-Ar ages of lava flows from the lower part of the Oxbow-Moteng Pass section (MP05-09, OXMQ, and MP07-09) cannot be statistically distinguished from the K-Ar age of sample NN57-m collected in the lowermost flow of the Naude's Nek section (Figure 10a).

The $^{40}Ar/^{39}Ar$ ages confirm that MP05-09 and MP07-09 from Oxbow-Moteng Pass section and NN45 from Naude's Nek section yield statistically similar ages (Figure 10b). The $^{40}Ar/^{39}Ar$ age of sample NN57-m differs, suggesting that the first lava flows were emplaced a few million years before the rest of the volcanic sequence (Figure 10b). The two $^{40}Ar/^{39}Ar$ ages (MP07-09 and MP05-09), from the lower part of the Oxbow-Moteng Pass section, are statistically younger than sample NN57-m but similar to sample NN45 at the 1σ level with a $(1/\sigma^2)$ weighted mean age of 181.3 ± 1.0 Ma (2σ) for these three ages. Comparison of K-Ar and $^{40}Ar/^{39}Ar$ ages shows reasonable agreement between the two techniques (Figure 10).

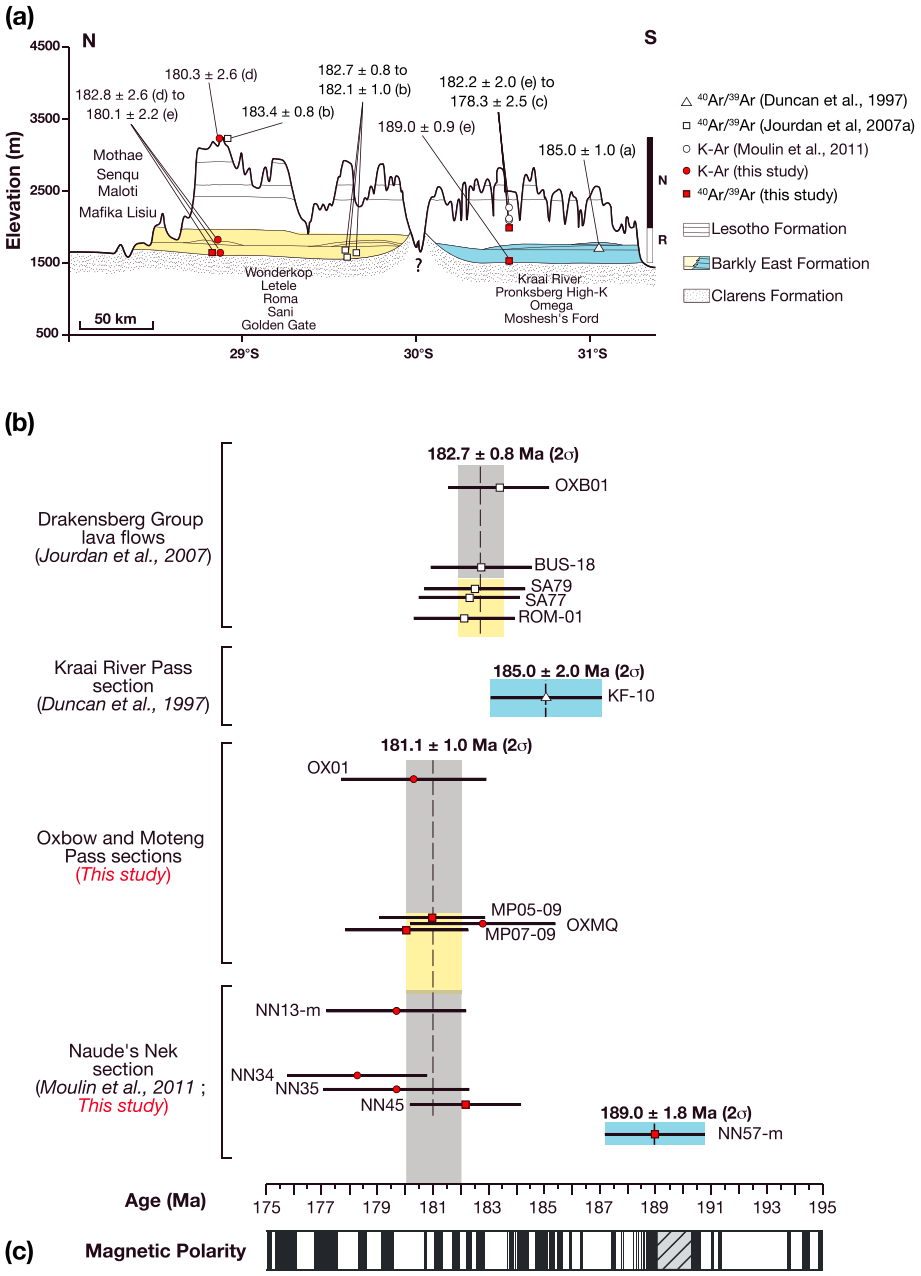

Figure 11. (a) Same as Figure 2, on which the new K-Ar [d] (shown by red circles) and $^{40}Ar/^{39}Ar$ [e] (shown by red squares) ages obtained in this paper have been added. (b) Summary of all $^{40}Ar/^{39}Ar$ (squares) and K-Ar (circles) ages obtained from mineral separates published in the literature and in this study (shown with a 1σ uncertainty). $^{40}Ar/^{39}Ar$ ages have been recalculated with an age of 28.201 Ma for the FCTs standard [*Kuiper et al.*, 2008]. The vertical dashed lines and shaded gray bands represent the weighted ($1/\sigma^2$) mean ages and uncertainties (at the 2σ level) for each subset respectively. Colors show geochemical formations in which samples were collected (see Figure 11a). (c) Geomagnetic polarity timescale from *Ogg et al.* [2008].

Only one of the nine K-Ar or $^{40}Ar/^{39}Ar$ ages can be considered as statistically discordant from the others, that is, the age of the first lava flow within the Naude's Nek section (NN57-m, which belongs to the Moshesh's Ford unit) at 189.0 ± 0.9 Ma (1σ) (Table 5). The average age of the rest of the lavas above (NN45, NN35, NN34, and NN13-m, collected within the Mafika Lisiu unit) and almost all of the Oxbow-Moteng Pass sequence (MP05-09 and maybe MP07-09, collected within the Letele unit, OX01 from the uppermost Mothae unit, and the sample OXMQ sampled in a dyke which has the geochemical signature of the Golden Gate unit) is 181.1 ± 1.0 Ma (2σ)

(Figure 11b). This ($1/\sigma^2$) weighted mean value (based on five K-Ar and three $^{40}Ar/^{39}Ar$ ages) is undistinguishable from the one obtained with K-Ar ages only (see Figure 10b). Based on these ages, the Naude's Nek volcanic sequence could have been emplaced in two successive phases (the lower one being far less voluminous than the upper) and volcanism in the Oxbow-Moteng Pass area was probably confined to the younger, main phase of activity.

We next compare the K-Ar and $^{40}Ar/^{39}Ar$ age determinations of our sections with previously reported $^{40}Ar/^{39}Ar$ ages from the Drakensberg group and with $^{40}Ar/^{39}Ar$ ages and U-Pb ages from dolerite sills and dykes. To avoid any bias induced by the use of whole-rock samples, we only consider hereafter $^{40}Ar/^{39}Ar$ ages obtained on mineral separates [e.g., *Hofmann et al*., 2000; *Jourdan et al*., 2007a]. All ages have been recalculated and are compatible with the new recommended age of 28.201 Ma for the FCTs standard [*Kuiper et al*., 2008] (Figure 11).

The $^{40}Ar/^{39}Ar$ age of 185 ± 2 Ma reported by *Duncan et al*. [1997] for the Omega unit (sample KF-10) (southern part of the Barkly East Formation) is compatible with our $^{40}Ar/^{39}Ar$ age from the Moshesh's Ford unit (sample NN57-m) but is also compatible with the mean age obtained for the whole Drakensberg group by *Jourdan et al*. [2007a] (Figure 11). The latter authors proposed that the discrepancy observed between older and younger ages could be attributed to excess $^{40}Ar^*$ and/or heterogeneity of standards. However, the age obtained by *Duncan et al*. [1997] can also be interpreted to support the existence of a brief phase of activity of minor importance in the southern part of the Drakensberg group at possibly ~189 Ma (which we hereafter refer to as Phase 1—P1—in Figures 13 and 14). We cannot confirm nor reject the hypothesis that the Omega unit belongs to the first phase of volcanism attested by sample NN57-m in the bottom part of the Naude's Nek section. Sample NN57-m belongs to the Moshesh's Ford unit, which is found only south of 30°S throughout the Naude's Nek and Barkly East areas (Figure 11a). The Moshesh's Ford unit was generally emplaced directly on the Clarens Formation. This first volcanic unit was followed by sandstone clastic deposits consisting in thin fluvial sandstone (<2 m thick), alone [*Marsh et al*., 1997; *McClintock et al*., 2008] or in association with volcaniclastic deposits representing possibly lahars, reaching locally tens of meters in thickness due to intense phreatomagmatic activity [*McClintock et al*., 2008]. The elapsed time represented by these volcaniclastic or fluvial deposits is largely unknown. However, this first volcanic period seems totally absent in Lesotho and even farther north of the Karoo basin. The Clarens depositional system remained active until about 183 Ma, when the second (major) volcanic phase began to erupt, in both the northern and southern parts of Lesotho.

Jourdan et al. [2007a] dated five plagioclase separates from three sections in the northern part of the Drakensberg group (ROM-01 and BUS-18 from the Bushmen's Pass section, SA77 and SA79 from the Sani Pass section, and OXB01 from the Oxbow section) that encompass almost the entire volcanic sequence (from the Golden Gate unit to the Mothae unit) (Figures 1b and 11). The five $^{40}Ar/^{39}Ar$ plateau ages yield a weighted mean of 182.7 ± 0.8 Ma (2σ) (Figure 11) [*Jourdan et al*., 2007a]. The three $^{40}Ar/^{39}Ar$ plateau and five K-Ar ages for the Oxbow-Moteng Pass section and upper part of the Naude's Nek section yield a weighted mean of 181.1 ± 1.0 Ma (2σ). This agrees at the 2σ level with Jourdan et al.'s ages (but the difference is not that small, 1.6 ± 1.8 Ma). The K-Ar age of 180.3 ± 2.6 Ma for OX01 (this work) is statistically similar at the 1σ level to the $^{40}Ar/^{39}Ar$ age of 183.4 ± 1.8 Ma for OXB01, collected in the same lava flow (the uppermost Oxbow section) by *Jourdan et al*. [2007a] (Figure 11). But again the difference for what must be the same real age is not small, at 3.1 ± 3.2 Ma. This underlines the fact that significant uncertainties remain, which can be partly due to changes in method, laboratory, standards, or experimental errors. The homogeneity of ages tends to suggest that the emplacement of the Barkly East Formation in the northern part of the Drakensberg group (from the Golden Gate unit upwards) and of the upper part of the volcanic pile (Lesotho Formation from Mafika Lisiu to Mothae units), therefore covering the whole of Lesotho (and likely much more prior to erosion), corresponds to a second *major* eruptive phase at ~181 ± 2 Ma (Phase 2—P2—in Figures 13 and 14). It corresponds to the main magmatic episode of the Karoo province and could have lasted 4 Ma [*Jourdan et al*., 2008] (but see below).

Uncertainties on $^{40}Ar/^{39}Ar$ ages, at best in the range of ±1.5 Myr, strongly limit our capacity to determine the actual timing and duration of emplacement of Drakensberg group lava flows. The use of the high-resolution U-Pb TIMS method to date zircons from the sills and dykes intruded in the Karoo sedimentary basin reduces the uncertainties on ages by 1 order of magnitude at least [*Svensen et al*., 2012; *Sell et al*., 2014]. The U-Pb

technique cannot be used to date mafic rocks that usually contain no zircons. Nevertheless, U-Pb dating of sills should provide a better estimate of the age and duration of emplacement of the Drakensberg group since there is clear evidence that sills intruding the Karoo sedimentary basin and lava flows of the Lesotho and southern part (south of 30°S) of Barkly East Formations are geochemically similar [*Galerne et al*., 2008, 2011; *Neumann et al*., 2011; *Svensen et al*., 2012]. *Svensen et al*. [2012] have dated 14 sills and dykes from the Karoo basin separated by as much as 1100 km by high-resolution U-Pb zircon TIMS method and obtained consistent ages (of crystallization), ranging from 183.0 ± 0.5 to 182.3 ± 0.6 Ma, indicating a brief emplacement in ~0.7 ± 0.6 Ma. This could indicate a single emplacement event (*Svensen et al*. [2012]; Figure 13). More recently, *Sell et al*. [2014] have dated baddeleyite and zircon crystals from a sill intruded in the Tarkastad Subgroup (Early Triassic) of the Karoo basin, using U-Pb TIMS. Its age is 183.02 ± 0.07 Ma, in good agreement with *Svensen et al*.'s [2012] ages (183.0 ± 0.5 Ma). The oldest age (of crystallization) has been obtained by *Burgess et al*. [2015], who dated the New Amalfi Sheet, a bowl-shaped intrusion, with U-Pb TIMS. They obtained a weighted mean age of 183.246 ± 0.045 Ma, within the uncertainty of *Encarnacion et al*. [1996] $^{206}Pb/^{238}U$ age (183.7 ± 0.6 Ma), suggesting that the New Amalfi Sheet was coeval with the inception of Phase 2, the major phase of magmatism in the Karoo LIP. *Svensen et al*. [2006] have shown that the formation of hydrothermal vent complexes in the Karoo Basin was synchronous with sill emplacement, slightly predating the major phase of Karoo flood basalt volcanism. This is consistent with slightly older ages obtained by *Jourdan et al*. [2008] for the Karoo sills compared to those obtained by *Jourdan et al*. [2007b] (with the same method and standard) for the Drakensberg group (Figures 13 and 14). U-Pb ages obtained by *Svensen et al*. [2012], *Sell et al*. [2014], and *Burgess et al*. [2015] for Karoo sills appear to be slightly younger than those acquired by *Jourdan et al*. [2008] using the $^{40}Ar/^{39}Ar$ method (~182–185 Ma) (Figure 13). The $^{40}Ar/^{39}Ar$ ages obtained by *Jourdan et al*. [2008] would suggest that the main sill events intruded in the Karoo sedimentary basin represent a magmatic event that could have lasted for ~3 Ma (Figure 13). This assumption is refuted by high-resolution U-Pb zircon TIMS ages [*Svensen et al*., 2012]. We therefore suggest that emplacement of the major phase P2 of the Lesotho Formation and of the intrusive complex in the Karoo Basin took place in the same brief interval, possibly as short as 0.5 Myr.

5.2. Constraints From Magnetic Chrons

Paleomagnetic analyses can provide higher-resolution estimates of the duration of volcanic phases, but they lack stratigraphic continuity. The Karoo lavas and sills were emplaced during a period of rather frequent magnetic reversals [e.g., *Ogg and Smith*, 2004] (Figure 11c). Uncertainties in $^{40}Ar/^{39}Ar$ age determinations (±1.5 Myr) combined with those due to the temporal calibration of the magnetic polarity timescale (MPTS —about 1.5 Ma for this period) prevent the unequivocal determination of precise correlations of the two volcanic phases with the MPTS. Lava flows of the first minor eruptive phase have recorded only reversed polarity at ~189 Ma. This is a time of strong variability in duration of reversed polarity chrons, suggesting a maximum range for eruption between less than a few tens of thousands of years and about 1 Myr (Figures 11b and 11c). The second major eruptive event (P2), dated at ~181 Ma (this work) and indirectly dated at 183 ± 0.6 Ma by sills [*Svensen et al*., 2012], has recorded a single magnetic reversal (within the Mafika Lisiu unit); the major part of lava flows (~90%) in this phase was erupted in a normal chron. Based on the MPTS, we estimate the duration of Phase 2 between 100 and less than 800 kyr: the major phase of activity possibly lasted much less than 800 kyr.

5.3. Constraints From Directional Groups

All detailed paleomagnetic sections available for the Drakensberg group are displayed in Figure 7. From north (left) to south (right), we have reported units with distinct magnetic directions (DGs or individual lava flows) obtained for the composite Oxbow-Moteng Pass (this study), Bushmen's Pass [*Prévot et al*., 2003], Sani Pass [*Kosterov and Perrin*, 1996], and Naude's Nek [*Moulin et al*., 2011] sections. In previous studies, magnetic directions were determined over only part of the section: the upper half (at the exception of the highest lava flows) along the Mafika Lisiu section [*Kosterov and Perrin*, 1996], one third of the Bushmen's Pass section [*Prévot et al*., 2003], and about one fifth of the Sani Pass section [*Kosterov and Perrin*, 1996] (Figure 7). In the present paper, we provide for the first time magnetic directions from the whole section. Mean magnetic directions of DGs from the Naude's Nek section [*Moulin et al*., 2011] have been recalculated, averaging magnetic directions at the sample rather than site level, in order to allow direct comparison with the other sections. As noted before (see section 3.2), this implies a decrease of the 95% confidence intervals but an

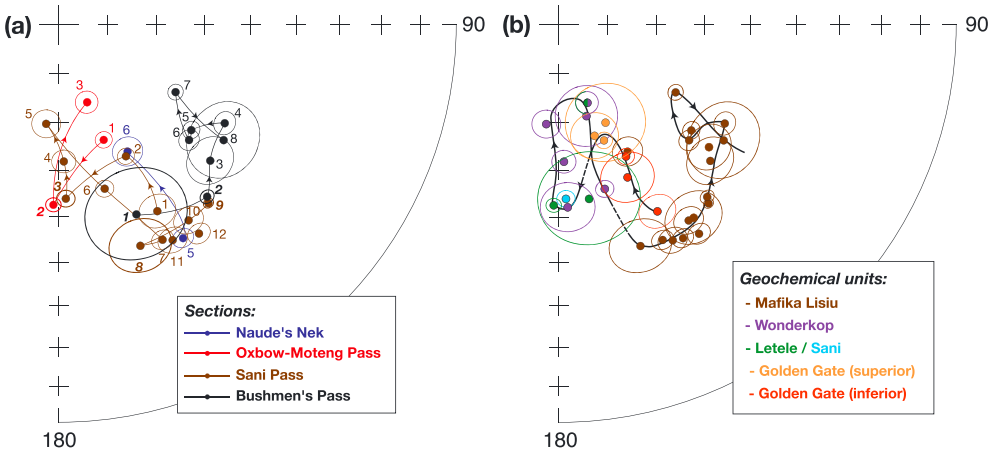

Figure 12. (a) Equal-area projection of distinct magnetic directions (directional groups and individual lava flows) of reversed polarity identified along the Naude's Nek section [*Moulin et al*., 2011], the Oxbow-Moteng Pass composite section (this study), the Sani Pass section [*Kosterov and Perrin*, 1996], and the Bushmen's Pass section [*Prévot et al*., 2003]. Numbering of magnetic directions is the same as the one of Figure 7. (b) Equal-area projection of the same (reversed) magnetic directions according to their corresponding chemical units (according to *Marsh et al*. [1997]). Eight magnetic directions obtained by *Rehacek* [1995] in the northern part of the Drakensberg group have been added.

insignificant variation of mean declinations and inclinations. A comparison of magnetic directions from one section to another allows one to identify lateral correlations: they are shown by lines (or dashed lines when we are less confident) in Figure 7.

5.3.1. Reversed Polarity

Magnetic directions with reversed polarity obtained for the Moshesh's Ford unit (bottom part of the Naude's Nek section), which correspond to the earlier minor eruptive phase, were not considered (Figure 7). Interestingly, the other reversed directions, recorded in the bottom part of the Drakensberg group, follow a rather consistent directional path (Figure 12a). The magnetic vector for the Sani Pass section (brown) follows a loop (directions 2 to 6) and then returns (direction 7) close to its original position. The path of the vector for the Oxbow-Moteng Pass section (red; directions 1 to 3) could correspond with the central part of the previous loop, but only magnetic direction 2 of the Oxbow-Moteng Pass section and magnetic direction 3 of the Sani Pass section can be clearly correlated (Figures 7 and 12a). The reversed trajectory continues with a series of three hairpins with ~140° amplitudes in declination (directions 7 to 12 of the Sani Pass section; direction 2 of the Bushmen's Pass section, in black; and direction 5 of the Naude's Nek section, in blue), followed by the excursional direction 6 of the Naude's Nek section (Figure 12a). Because of a large confidence interval, the first direction of the Bushmen's Pass section cannot be constrained in the directional path. The following directions (3 to 8) at Bushmen's Pass probably correspond to the last magnetic directions with full reversed polarity below the reversal.

Paleomagnetic (secular variation) analysis of reversed directions therefore allows us to connect sections in logical order and therefore to propose a relative chronology of emplacement of lava flows. The first lava flows of the Moteng Pass section were emplaced simultaneously with the first lava flows in the Sani Pass area, shortly after the beginning of volcanic activity (at Sani Pass) (Figure 7). Emplacement of the upper part of the Sani Pass section was contemporaneous with emplacement of the lowermost lava flows in the Naude's Nek section. The major part of lava flows from the Bushmen's Pass section was emplaced just after this. This relative chronology agrees with the chemical division of the Drakensberg group proposed by *Marsh et al*. [1997] (Figure 2) and allows us to provide new constraints on the eruptive history of the northern part of the Barkly East Formation. Indeed, if we label reversed magnetic directions as a function of chemical units (Figure 12b), we can conclude the following:

1. The Golden Gate unit has likely been emplaced in two phases, in agreement with the geochemical division proposed by *Rehacek* [1995], with eruption of the lower Golden Gate unit followed by rapid eruption of the upper Golden Gate unit.

2. After some (probably very short) time, the Sani unit in the Sani Pass area and the major part of the Letele unit further north in the Oxbow-Moteng Pass area were emplaced quickly and simultaneously.
3. The eruption of the Wonderkop unit began immediately afterward and continued for some time.
4. In the lower part of the Moteng Pass section, the boundary between the Letele and Wonderkop units is included in the directional group DG-OM3 (Figure 7), suggesting that the onset of emplacement of the Wonderkop unit was simultaneous with outpouring of the last lava flows of the Letele unit.
5. Finally, after an undetermined length of time, eruption of the Mafika Lisiu unit (the first chemical unit of the Lesotho Formation) started.

These observations are consistent with previous work [*Mitha*, 2006; *McClintock et al*., 2008] and show that eruptions of chemically distinct magmas can take place over (very) short intervals of time, and even be quasi-simultaneous. This holds not only for chemical units of the Barkly East Formation. Two directional groups (DG-OM19 and DG-OM21) that occur in the Maloti unit, in the upper part of the Moteng Pass section, are also found, but the same groups belong to the Senqu unit in the lower part of the Oxbow section. Emplacement of the latest Maloti and first Senqu lava flows was likely contemporary.

5.3.2. Transitional Polarity

The van Zijl magnetic reversal, the only one recorded by volcanism in Lesotho, has been found in three volcanic sections (Bushmen's Pass [*Prévot et al*., 2003] and Naude's Nek and Oxbow-Moteng Pass [*Moulin et al*., 2011, 2012]; Figure 7). Two or three characteristic transitional paleomagnetic directions have been identified in different sections (Figure 7). For more details, one can find a reconstruction of the VGP reversing path in *Moulin et al*. [2012].

A paleomagnetic study by *Ward et al*. [2005] in the Karoo Basin (sediments and dolerite dyke) may actually allow us to correlate emplacement of the intrusive complex with phase P2. Indeed, the magnetic direction obtained for dykes ($D = 117.4°$, $I = 13.6°$, $\alpha_{95} = 3.7°$) [*Ward et al*., 2005] is very close to the directions we find for samples MP15, MP16, and MP17 (DG-OM5) (Tables 1 and 2). This is a unique, very characteristic magnetic direction recorded by lava flows during the van Zijl reversal.

5.3.3. Normal Polarity

Above the reversal, we discuss chemical units separately. Normal lava flows all occur within the Lesotho Formation (Figure 2). Three lava groups in the three normal magnetic records in the Mafika Lisiu unit have comparable magnetic directions (and two correlations are less reliable) (Figure 7). These lateral correlations are observed over large distances (~200 km), from south (Naude's Nek section) to north (Oxbow-Moteng Pass section), also involving Bushmen's Pass (Figure 1b). An even larger number of paleomagnetic correlations are identified between the Oxbow-Moteng Pass and Mafika Lisiu sections, separated by only ~50 km (Figure 1b). A total of 11 pairs of directional groups (including three less certain ones) have been matched between the two sections (Figure 7). Recall that DGs are interpreted as a signature of cooling times of single eruptive events shorter than 100 and possibly 10 years.

The angular standard deviation (ASD) of paleomagnetic poles from a given site or a DG is generally used to characterize the dispersion due to secular variation. The ASD for all VGPs (based on distinct normal and reversed directions) for the Naude's Nek and Oxbow-Moteng Pass sections is 15.5°. This is consistent with the 14.1° obtained by *Kosterov and Perrin* [1996] for the Drakensberg group, with the 16° recently determined by *Biggin et al*. [2008] for the Jurassic and (taking into account the paleolatitude of −38° for Lesotho; this study) with the ~17° value for the same latitude band for the past 5 Ma [*McFadden et al*., 1991; *Quidelleur and Courtillot*, 1996].

Following *Chenet et al*. [2008] and earlier Karoo province results [*Moulin et al*., 2011], we consider that DGs have cooled in no more than ~100 years. This is valid only for DGs of normal or reversed polarity. Because dipole field intensity is generally lower during a reversal, the (nondipole) variation rate could have been significantly larger during the van Zijl reversal than during full polarities [*Valet et al*., 2012; *Moulin et al*., 2012]. This could imply that the characteristic size of DGs erupted during the reversal was significantly larger and that corresponding pulses of lava were emplaced in even less than a century.

Twenty magnetic correlations between lava flows have been identified across the Drakensberg group (Figure 7). Paleomagnetic sampling of the group is not exhaustive: we can estimate an effective duration of volcanic activity at a given locality but not at the scale of the province. The duration of volcanic activity for the first minor eruptive phase identified in the lower part of the Naude's Nek section (Moshesh's Ford

unit), which comprises only four directional groups (Figure 7), could have been a few hundred years (4 times 100 years). The fact that 25 and 37 individual, distinct magnetic directions (directional groups or individual lava flows) were observed for the second major eruptive phase along the Naude's Nek and Oxbow-Moteng Pass sections, respectively (Figure 7), implies that the total time of volcanic activity may not have exceeded ~4000 years. These estimates do not include possible periods of quiescence between flows corresponding to distinct magnetic directions and hence do not provide the total duration of eruption. Although we cannot precisely calculate the duration of inactive periods, we can estimate their relative magnitude. Because the duration of a reversal is on the order of 10^4 years [e.g., *Clement*, 2004] or less [*Valet et al*., 2012], effective volcanic activity may reflect between 10% and 20% (and possibly much more) of the duration required for the emplacement of the volcanic sequence during the reversal (the Oxbow-Moteng Pass, Bushmen's Pass, and Naude's Nek sections respectively show 8, 21, and 10 distinct magnetic directions within the reversal, which could correspond to an effective time of volcanic activity between about 1000 and 2000 years). Since we do not know whether the eruption rate changed over time, we cannot extrapolate these values to the rest of the volcanic sequence. We suggest that quiescence periods are not necessarily important and that the emplacement of the entire Lesotho Formation (about 90% of the total Drakensberg group volume) could correspond to a very short period (<40,000 years?).

6. From the Drakensberg Group to the Whole Karoo-Ferrar LIP?

We next compare our geochronologic results with other age determinations of Karoo and Ferrar basalts available in the literature, in order to see whether some of the results obtained in Lesotho can be extended to the whole LIP. A total of 178 ages on mineral separates (mainly $^{40}Ar/^{39}Ar$, but also U/Pb and K-Ar) are available for the Karoo-Ferrar LIP (Figures 13 and 14). All $^{40}Ar/^{39}Ar$ ages have been recalculated relative to the age of 28.201 Ma for the FCTs standard [*Kuiper et al*., 2008]. However, the reliability of some standards used for $^{40}Ar/^{39}Ar$ has been questioned (for instance, heterogeneity of the FCT-3 biotite standard used by *Duncan et al*. [1997], *Jones et al*. [2001], and *Riley et al*. [2006]; see *Jourdan et al*. [2007a]). In addition, absolute ages of flux monitors, as well as the exact value of the K decay constants, remain debated [*Kuiper et al*., 2008; *Renne et al*., 2010].

The oldest lava flows are encountered in the southern part of the Drakensberg group (Moshesh's Ford unit) at ~189 Ma (Figures 9–11). This corresponds to a possible first emplacement stage of the Karoo province as defined by *Jourdan et al*. [2008]. This first magmatic phase (P1 in Figures 13 and 14) is brief and of minor importance. The sandstone clastic deposit above the Moshesh's Ford unit consists of fluvial sandstone (<2 m thick) alone or in association with volcaniclastic deposits (locally reaching tens of meters in thickness). To the north of 30°S, there is no evidence for this early phase in the Karoo basin. The precise length of the following period of quiescence remains poorly constrained.

The emplacement of phase P2 (Figures 13 and 14) a few million years later at ~181–183 Ma corresponds to emplacement of the Barkly East Formation in the northern part of the Drakensberg group (from the Golden Gate unit upwards) and of the upper part of the volcanic pile (Lesotho Formation from Mafika Lisiu to Mothae units), therefore covering the whole of Lesotho (and likely much more prior to erosion). It corresponds to the main magmatic episode of the Karoo province. $^{40}Ar/^{39}Ar$ and K-Ar ages have large uncertainties and are compatible with a single volcanic phase. Based on the geochemical similarities of the Karoo basin intrusive complex with the Lesotho Formation and on the U-Pb TIMS ages on zircons from sills [*Sell et al*., 2014], we suggest that emplacement of the Lesotho Formation (representing about 90% in thickness of the lava flows outcropping along the Oxbow and Moteng Pass sections) may have lasted as little as 0.5 Myr. The northern part of the Barkly East Formation may not have been emplaced within this 0.5 Myr long period. It is geochemically different from the Lesotho Formation. In that case, there is no good constraint on the time elapsed between the Barkly East Formation and the Lesotho Formation.

The record of a single reversal (R-N) and the presence of a single normal magnetozone in the upper 1000 m thick volcanic pile in Lesotho sections support very rapid emplacement of the whole Drakensberg group. Indeed, seven reversals have been recorded during the first two ammonite biozones (*Tenuicostatum* and *Falciferum*) of the Toarcian [*Ogg and Smith*, 2004; *Iglesia Llanos*, 2012] that could be as short as 1.7–1.9 Myr [*Boulila et al*., 2014; *Ikeda and Hori*, 2014], i.e., a rate of four reversals per million year. Assuming a constant reversal rate, the duration of the normal magnetozone would not have exceeded ~250 kyr. The reversed

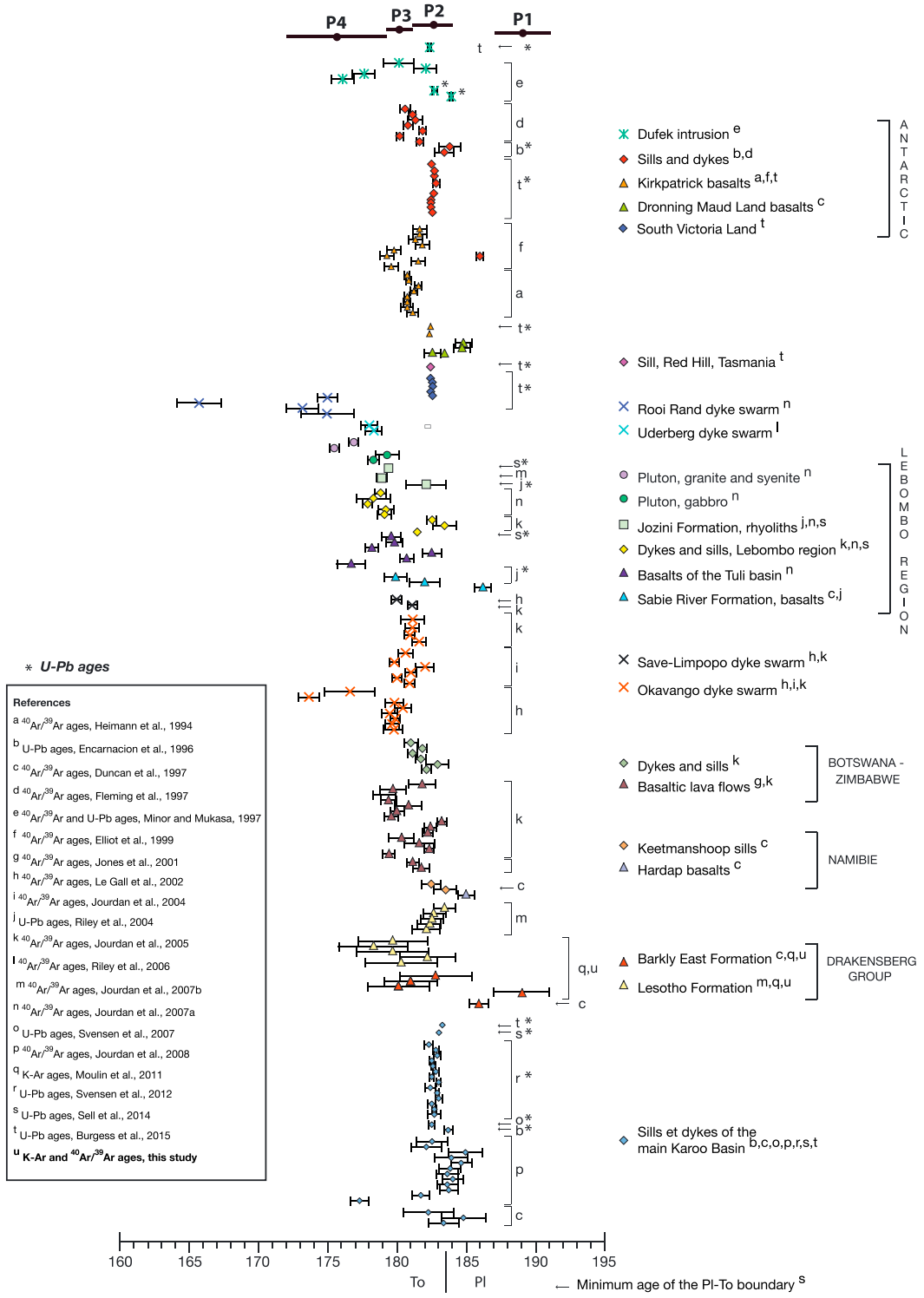

Figure 13. Compilation of 178 mineral separate $^{40}Ar/^{39}Ar$ (125), U/Pb (48), and K-Ar (5) ages (at the 1σ level) obtained for the Karoo-Ferrar magmatic province. All $^{40}Ar/^{39}Ar$ are intercalibrated using the new recommended age of 28.201 Ma [*Kuiper et al.*, 2008] for the FCTs standard. We define four eruptive phases (P1 to P4; see text). Phase P1 is of minor importance and possibly of short duration; Phase 2 coincides with the major environmental and climatic perturbations, suggesting that it is related to the emplacement of the main part of the Karoo basalts and the release of large amounts of volcanic and thermogenic gases. Phase 2 may be divided into two subphases to fit the environmental events (see discussion). Phase 3 corresponds to moderate volcanic activity. Phase 4 represents the final period of volcanism, stretching from 179 to 175 Ma, mainly observed in Lebombo (South Africa) and Ferrar (Antarctica).

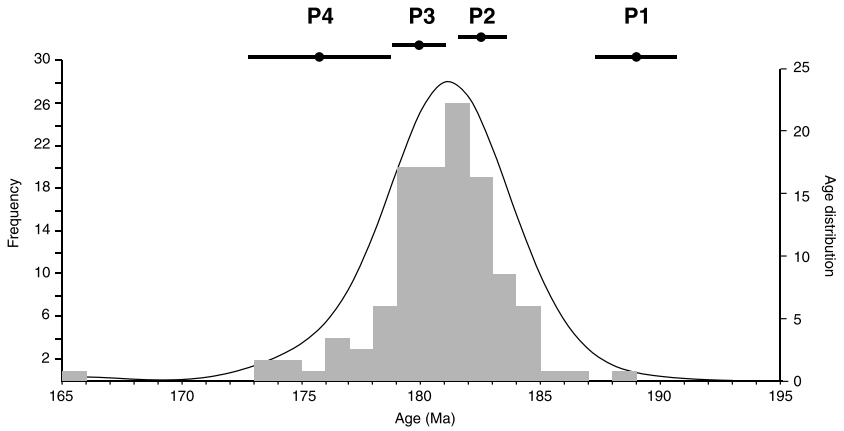

Figure 14. $^{40}Ar/^{39}Ar$ age probability density distribution diagram and frequency histogram of 125 rocks of the Karoo-Ferrar province [*Heimann et al*., 1994; *Duncan et al*., 1997; *Fleming et al*., 1997; *Minor and Mukasa*, 1997; *Elliot et al*., 1999; *Jones et al*., 2001; *Le Gall et al*., 2002; *Jourdan et al*., 2004, 2005, 2007a, 2007b, 2008; *Riley et al*., 2006; and this study]. Volcanic phases P1 to P4 described in the text are roughly indicated.

magnetozone recorded by lava flows belonging to the Barkly East Formation that appears at the base of the Naude's Nek and Moteng Pass sections (<100 m) and is better exposed farther southeast in Sani Pass [*Kosterov and Perrin*, 1996] shows that volcanism started earlier in that area.

Combining absolute ages with geochemical and paleomagnetic data, *Marsh et al*. [1997], *Hargraves et al*. [1997], *Duncan et al*. [1997], and *Marsh* [2016] have proposed that the emplacement of the Springbok Flats volcanic sequence, Namibia lavas (Hardap section of the Kalkrand Basalt Formation and Keetmanshoop dolerite sills), the lower part of the Lebombo sequence (Sabie River Formation), and the latest stratigraphic unit of the Suurberg Group in the Algoa Basin (Mimosa basaltic formation) could be contemporaneous with the emplacement of the Drakensberg group (except for the Moshesh's Ford unit), that is to say, with the "Phase 2" that we identified (Figure 11a). The Batoka basalts exposed in the northwestern part of the Karoo province (Zimbabwe) dated at 180 Ma have recorded a normal polarity and seem chemically correlated with the upper part of the Sabie River Formation (Lebombo) [*Jones et al*., 2001] (Figure 1a). Part of the northern lavas outcropping in Botswana and Zimbabwe could therefore also have been emplaced during the same normal chron recorded by Phase 2 of the Drakensberg group.

Jourdan et al. [2007a] have identified brief (~1 Myr or less), temporally distinct events: the Okavango dyke swarm, the 800 m thick southern Botswana Shadi-Shadi lava pile, and the Lesotho lava pile (Figures 1a, 13, and 14). Although the mean emplacement ages of the Okavango dyke swarm (180.3 ± 0.2 Ma) and southern Botswana lavas (179.7 ± 0.3 Ma) differ (the 1σ ranges fail to intersect by only 0.1 Ma), all ages have the same range: 179.2 ± 0.5 to 182.0 ± 0.7 Ma for Okavango [*Le Gall et al*., 2002; *Jourdan et al*., 2004, 2005] and 179.1 ± 0.8 to 181.8 ± 1.0 Ma for southern Botswana [*Jourdan et al*., 2005], suggesting that these two magmatic events could actually correspond to a single volcanic phase. Thus, the Okavango and Save Limpopo dyke swarms, plus part of the northern basalts in Botswana and Zimbabwe, could correspond to a third eruptive event (~180 Ma) (Phase 3), occurring slightly after the emplacement of the Drakensberg group (Phase 2).

Finally, the youngest magmatism (~175–180 Ma), which is not found in the Drakensberg group, is encountered in the Lebombo region, namely, the rhyolite formations and plutonic complexes [*Jourdan et al*., 2007a; *Sell et al*., 2014]. These volcanics erupted in a rift setting, approximately 2 Myr after the major phase of Karoo magmatism [*Sell et al*., 2014].

Magmatism is not restricted to the African continent. The lava flows and intrusive complexes of the Dronning Maud Land magmatic province in Antarctica are now separated from the African continent by the southwest Indian Ocean yet are related to the Karoo lava flows as indicated by strong geochemical affinities, particularly with the Sabie River unit [*Harris et al*., 1990] and by comparable ages [*Duncan et al*., 1997]. Other volcanic units encountered in Antarctica belong to the Ferrar province, which is contemporaneous with the main phase of the Karoo province [*Heimann et al*., 1994; *Encarnacion et al*., 1996; *Fleming et al*., 1997; *Minor and Mukasa*, 1997; *Elliot et al*., 1999; *Riley and Knight*, 2001]. High-resolution U-Pb ages of sills and flows from

the Central Transantarctic Mountains [*Burgess et al*., 2015] fall within the range of *Sell et al*.'s [2014] Karoo sill ages.

In summary, the total duration of Karoo-Ferrar LIP magmatism was ~10–15 Ma (Figures 13 and 14), during which several peaks of activity have been identified. Following a first, probably brief event at ~189 Ma (P1), the main magmatic (basaltic) episode could have lasted 3 Ma, around 181–183 Ma (Figures 13 and 14) [*Jourdan et al*., 2008]. We propose that this phase consisted of two distinct magmatic pulses.

1. A first one (P2) is at about 183 Ma, including the main part of the Drakensberg group (except for the Moshesh's Ford unit), the Karoo intrusive complex, the Springboks Flats sequence, the Namibia lavas, a part of the northern basalts from Botswana and Zimbabwe and of the Sabie River Formation (Lebombo), and the Ferrar volcanism in Antarctica and Tasmania. Based on geochemical correlation between the intrusive complex and the Lesotho Formation and paleomagnetism, the P2 phase could have been as short as 250 kyr (the northern part of the Barkly East Formation representing a minor volume compared to the Lesotho Formation may have been emplaced shortly before).
2. Another one (P3) is a few million years later (~180 Ma) (including the Okavango and Save Limpopo dyke swarms, plus part of the northern basalts in Botswana and Zimbabwe). Volcanism of the Karoo-Ferrar province ended with a minor activity phase (P4, roughly between 173 and 179 Ma) in the Lebombo region and in the Rooi Rand dike swarm, respectively [*Jourdan et al*., 2007b].

Paleomagnetic observations of a lack of secular variation in successive flows (DGs and SEEs) provide the main constraints that allow us to argue that volcanism was of a pulsed nature, with remarkably short and intense pulses during Phase 2. The duration of some of these pulses was likely some 4 orders of magnitude smaller than uncertainties on high-resolution U-Pb absolute ages.

7. The Karoo-Ferrar LIP and the Pliensbachian-Toarcian Extinctions

The temporal coincidence between emplacement of the Karoo-Ferrar LIP and environmental perturbations near the Pliensbachian-Toarcian boundary has led a number of authors to argue in favor of a causal connection between the two events [e.g., *Duncan et al*., 1997; *Pálfy and Smith*, 2000; *Guex et al*., 2001; *Courtillot and Renne*, 2003; *Svensen et al*., 2007; *Jourdan et al*., 2008; *Guex et al*., 2012; *Caruthers et al*., 2013, 2014; *Ikeda and Hori*, 2014; *Sell et al*., 2014]. Taken together, the geochronologic and paleomagnetic constraints on eruptive history of the Karoo LIP and the patterns revealed by the geochemical and paleontological records of Pliensbachian-Toarcian times allow us to propose an eruptive scenario leading to multiphased extinctions. The climate disruptions were controlled by the (precise) timing and volumes (hence fluxes) of gases emitted by successive volcanic pulses. These occurred in a series of embedded timescales [*Courtillot and Fluteau*, 2014]: overall, volcanism lasted on the order of 10–15 Myr between the first and last manifestations of volcanic activity. However, volcanism appears to have been concentrated in a few ~1 Myr (or less) major magmatic phases. Each phase itself consisted of possibly 100 kyr (or less) events, themselves formed of successions of single eruptive events having lasted less than a century (possibly down to a decade). Despite the insufficient precision of absolute age determinations (with the exception of a few samples [*Sell et al*., 2014]), one can combine these determinations with the observations from geochemistry, sedimentology, paleontology, and the new paleomagnetic data to propose a scenario that may not be unique but fits most observations.

A first magmatic phase P1 (Figure 15) dated at about 189 ± 2 Ma [this work; *Jourdan et al*., 2007a] may be coeval with a first perturbation of the carbon cycle and the noticeable decline in ammonite diversity at the *Ibex*/*Davoei* zone boundary, mainly in the northwest Tethys and Boreal Oceans [*Caruthers et al*., 2013]. A second decline in biodiversity, affecting ammonites and foraminifera, occurred in the late Pliensbachian (in the *Margaritatus* and *Spinatum* zones) and is coeval with a global cooling and marine regression.

A third drop in biodiversity straddles the Pliensbachian/Toarcian boundary and reaches its minimum at the *Tenuicostatum-Falciferum* limit. This double event corresponds to the acme of the biodiversity crisis of both microfauna and macrofauna [*Dera et al*., 2011; *Caruthers et al*., 2013, 2014]. The two events are coeval with global warming, strong perturbations of the carbon cycle, and marine anoxia. Based on dating and identification of a peculiar magnetic direction, we conclude that the emplacement of a very large fraction of the Karoo volcanism (notably the Drakensberg group) coincided with these major environmental perturbations and is

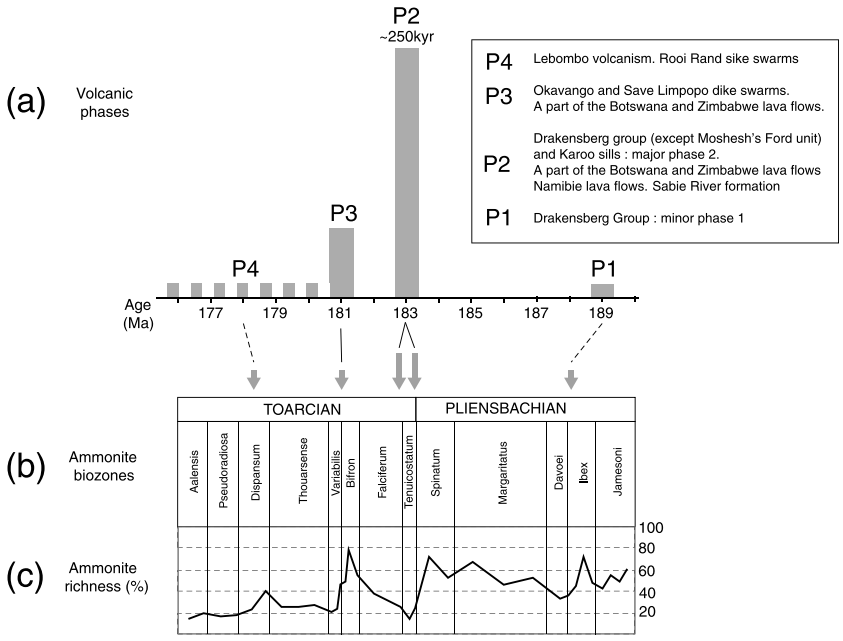

Figure 15. (a) The eruptive scenario proposed for the volcanic province (see text for more details). Possible correlations between crises and environmental perturbations linked to emplacement of the Karoo-Ferrar province near the Pliensbachian-Toarcian boundary. Height and width of rectangles represents roughly the importance and duration of the volcanic activity respectively. (b) Paleontological ammonite zones. (c) Variations in ammonite species richness.

their most likely cause. The presence of a single magnetic reversal within the whole volcanic sequence supports a scenario in which the Drakensberg group was emplaced rapidly. The evidence for a double extinction event would imply that environmental stress induced by magmatic activity in the Karoo may have fluctuated over that period (Phase 2).

The narrow time frame in which both the volcanism and the CIE (Figure 15) occurred, both lasting of the order of a few thousand years (may be less), naturally lead one to suggest that emplacement of the Drakensberg group drove the Early Toarcian perturbations. Indeed, massive and repeated injections of CO_2 in the atmosphere due to volcanism (aerial flows and sills) could have led to the rise of pCO_2 and subsequent global warming recorded in the *Tenuicostatum*/*Falciferum* biozones [*McElwain et al*., 2005]. Assuming an average concentration of sulfur and carbon dioxide in basaltic magmas similar to those in the Deccan traps (1000 ppm of SO_2 and 0.5% of CO_2 [*Self et al*., 2006]), one can estimate the total release of SO_2 at about 6000 Gt and CO_2 at about 14,000 Gt per million cubic kilometers of basalt during LIP emplacement [*Chenet et al*., 2009]. The original volume of the Karoo-Ferrar magmatic event, estimated at $\sim 2.5 \times 10^6$ km^3 [*Cox*, 1988; *Encarnacion et al*., 1996], implies the possible release of 15,000 Gt of SO_2 and 35,000 Gt of CO_2. *Svensen et al*. [2007] estimated that an additional release of 27,400 Gt of CO_2 could have been produced by sill intrusion in the organic shale of the Karoo Basin. Thus, ~60,000 Gt of CO_2 ($\sim 16 \times 10^{18}$ g of carbon) could have been injected into the atmosphere over a period as short as 0.5 Myr (Phase P2). The magmatic phase (P2) seems to coincide with the two main peaks of mass extinctions and abrupt environmental changes of the end Pliensbachian and Early Toarcian [*Guex et al*., 2012].

Outbursts of CO_2 pulses corresponding to peaks of volcanic and subvolcanic activities or massive emission of thermogenic gases (CH_4) or both can explain the abrupt global warming observed during the early Toarcian [e.g., *Svensen et al*., 2006, 2007; *Aarnes et al*., 2011; *Dera et al*., 2011; *Hermoso et al*., 2012]. Following the acme of temperature, there is a warm period (~2 Myr) from the *Falciferum* to the *Variabilis* ammonite biozones (ammonite zone duration estimates from GTS2004 [*Ogg and Smith*, 2004]). This may be linked with the persistence of high atmospheric pCO_2 due to the continuation of Karoo-Ferrar volcanic activity (though it was then much less intense). Because of higher temperatures and greater precipitation, silicate weathering should have been enhanced, leading to a decrease of pCO_2 and subsequent cooling [*Dessert et al*., 2001].

However, the Karoo LIP was formed at a paleolatitude of 38°S ± 4° (this work); the underlying eolian sandstone of the Clarens formation suggests an arid climate [*Bordy and Catuneanu*, 2002]. If precipitations (and runoff) had not drastically varied in response to the rise of pCO_2, the weathering of Karoo basalts and, as a consequence, the consumption of CO_2 could have been limited, failing to draw atmospheric pCO_2 down within the following hundreds of thousands of years. The release of large amounts of CO_2 may also have favored marine anoxia due to a decline in oceanic circulation and acidification of the surface ocean, leading to a crisis in the biosphere and decline in biodiversity. The negative CIEs recorded at the end Pliensbachian and Early Toarcian suggest that huge amounts of ^{13}C-depleted carbon were injected into the atmospheric and superficial oceanic reservoirs [*McElwain et al*., 2005]. The source of ^{13}C-depleted carbon can be thermogenic methane produced by magmatic intrusion in the Karoo sedimentary basin [*McElwain et al*., 2005; *Svensen et al*., 2007] and/or emissions of volcanogenic CO_2 [*Suan et al*., 2008]. The release of ^{13}C-depleted carbon might have been related to paroxysmal magmatic activity. The emission of a large amount of SO_2 released by Karoo volcanism would have caused brief cooling events lasting a few tens of years [*Mussard et al*., 2014]. Unfortunately, such cold events cannot be recorded because of their brevity, but they may have influenced the chemistry of the ocean through acidification and a rise of the lysocline [*Mussard et al*., 2014; *Fluteau and Le Hir*, 2014]. The minor declines in biodiversity recorded during the Late Toarcian affected some groups specifically. They may have been linked to the late phases of volcanic activity known in the Karoo and Ferrar magmatic provinces: the *Bifrons*/*Variabilis* zone boundary crisis with volcanic Phase 3 (P3 on Figures 13 and 15) in Okavango and Save Limpopo and the *Dispansum* zone crisis with volcanic Phase 4 (P4 on Figures 13 and 15) in Lebombo and Rooi Rand.

Although the absolute ages of the different magmatic phases of the Karoo-Ferrar and of the multiple Pliensbachian to Toarcian crises and environmental perturbations are not accurate enough to demonstrate a one-to-one correlation among all these events, the results reported in this paper and in *Moulin et al*. [2011] lead us to propose that the main volume of the Karoo-Ferrar LIP was emplaced in a small number of paroxysmal phases with a duration that probably did not exceed a few 10^4 years or even less. This emplacement chronology is in good agreement with the discontinuous rhythm of environmental and biotic perturbations in the Pliensbachian-Toarcian interval, with the acme of volcanism occurring in two discrete phases at the Pliensbachian-Toarcian boundary and *Tenuicostatum-Falciferum* biozones. A causal relationship between Karoo-Ferrar LIP emplacement and crises and environmental instabilities recorded during the Pliensbachian-Toarcian interval is supported by the present study.

8. Conclusion

In this paper, we have reported new paleomagnetic and geochronologic results from the ~1500 m thick Oxbow-Moteng Pass composite section in the northern part of Lesotho where Karoo lavas are (almost) the thickest. These analyses supplement those obtained by *Moulin et al*. [2011] for the lower 800 m of lava flows at Naude's Nek (South Africa). New age determinations (K-Ar Cassignol-Gillot and $^{40}Ar/^{39}Ar$ techniques) range between 180.1 ± 1.4 and 182.8 ± 2.6 Ma and show that most if not all of the volcanism in the Oxbow-Moteng Pass area probably occurred within ~2 Myr (unfortunately with a large uncertainty) in a small number of phases of major activity. New ages from the lowermost part of the Naude's Nek section confirm that the first lava flows were emplaced a few million years before the rest of the volcanic sequence [*Moulin et al*., 2011].

Volcanism of the Drakensberg group occurred in two brief (<1 Myr, probably much less) successive phases. The first (minor) activity phase (corresponding to the Moshesh's Ford unit) amounts to about 10% of the total volume and is found only in the southern part of the Drakensberg. It erupted at ~189 Ma, entirely within a reversed magnetic chron. Comparison with the geomagnetic reversal timescale allows for a duration of up to 1 Myr, but volcanism probably occurred in only a few tens of thousands of years, maybe even much less. The second phase, comprising about 90% of the total volume, began in a reversed chron and recorded a single reversal and the beginning of a normal chron, around 183–181 Ma. This phase is by far the largest. Its total duration could have been as short as 250 kyr (the mean duration of a chron during the Early Toarcian), possibly again much less. This magmatic event coincides with the intrusions of sills and dykes within the Karoo sediments. On a shorter timescale (<1 kyr), the analysis of secular variation allows us to show that the province was constructed in a succession of single eruptive events having lasted less than a century.

Detailed flow-by-flow magnetostratigraphy shows that the composite Oxbow-Moteng Pass section can be divided into 37 distinct magnetic directions, comprising 21 directional groups and 16 individual lava flows, and the Naude's Nek section into 29 directions, comprising 19 directional groups and 10 individual lava flows. We therefore propose that the eruptive period, corresponding to the total duration of lava flow emplacement but excluding periods of quiescence between lava flows, did not exceed a few centuries for Phase 1 and a few millennia for Phase 2.

Combined analysis of available geochronologic, paleomagnetic, and geochemical data from the entire Karoo-Ferrar LIP allows an improved (if still tentative) reconstruction of its eruptive history. This emplacement chronology is in good agreement with the discontinuous rhythm of environmental and biotic perturbations during the late Pliensbachian-Toarcian interval. Pulsed emissions of volcanic gases could have been the main trigger of the multiple phases of extinction advocated by *Dera et al*. [2010] and *Caruthers et al*. [2013]. The ensemble of available data is consistent with a scenario in which the two main phases of extinction at the Pliensbachian-Toarcian boundary and *Tenuicostatum*/*Falciferum* zone boundary corresponded to the largest pulse (Phase 2) of volcanism, have possibly lasted a short time, on the order of 100 kyr or less.

Acknowledgments

We thank Robert Duncan and Henrik H. Svensen for their thorough and constructive review of this manuscript. We are grateful to Hélène Bouquerel for technical and field assistance. Funding was obtained through the CNRS !KHURE AFRICA French-South African joint research program. The data used are listed in the references, tables, and supplements. This is IPGP contribution 3809.

References

Aarnes, I., H. Svensen, S. Polteau, and S. Planke (2011), Contact metamorphic devolatilization of shales in the Karoo Basin, South Africa, and the effects of multiple sill intrusions, *Chem. Geol.*, *281*, 181–194.

Al-Suwaidi, A. H., G. N. Angelozzi, F. Baudin, S. E. Damborenea, S. P. Hesselbo, H. C. Jenkyns, M. O. Manceñido, and A. C. Riccardi (2010), First record of the Early Toarcian Oceanic Anoxic Event from the Southern Hemisphere, Neuquén Basin, Argentina, *J. Geol. Soc. London*, *167*, 633–636, doi:10.1144/0016-76492010-025.

Bailey, T. R., Y. Rosenthal, J. M. McArthur, B. van de Schootbrugge, and M. F. Thirlwall (2003), Paleoceanographic changes of the Late Pliensbachian-Early Toarcian interval: A possible link to the genesis of an oceanic anoxic event, *Earth Planet. Sci. Lett.*, *212*(3–4), 307–320, doi:10.1016/S0012-821X(03)00278-4.

Besse, J., and V. Courtillot (2002), Apparent and true polar wander and the geometry of the geomagnetic field over the last 200 Myr, *J. Geophys. Res.*, *107*(B11), 2300, doi:10.1029/2000JB000050.

Biggin, A. J., D. J. J. van Hinsbergen, C. G. Langereis, G. B. Straathof, and M. H. L. Deenen (2008), Geomagnetic secular variation in the Cretaceous Normal Superchron and in the Jurassic, *Phys. Earth Planet. Inter.*, *169*, 3–19, doi:10.1016/j.pepi.2008.07.004.

Bond, D., and P. Wignall (2014), Large igneous provinces and mass extinctions: An update, In *Volcanism, Impacts and Mass Extinctions: Causes and Effects*, *Geol. Soc. Am*., SP505, edited by G. Keller and A. Kerr. pp. 29–56, Boulder, Colo., doi:10.1130/2014.2505(2).

Bordy, E. M., and O. Catuneanu (2002), Sedimentology and palaeontology of upper Karoo aeolian strata (Early Jurassic) in the Tuli Basin, South Africa, *J. Afr. Earth Sci.*, *35*, 301–314, doi:10.1016/S0899-5362(02)00103-3.

Boulila, S., B. Galbrun, E. Huret, L. A. Hinnov, I. Rouget, S. Gardin, and A. Bartolini (2014), Astronomical calibration of the Toarcian Stage: Implications for sequence stratigraphy and duration of the early Toarcian OAE, *Earth Planet. Sci. Lett.*, *386*, 98–111, doi:10.1016/j.epsl.2013.10.047.

Brewer, T. S., D. Rex, P. G. Guise, and C. J. Hawkesworth (1996), Geochronology of Mesozoic tholeiitic magmatism, in *Antarctica: Implications for the Development of the Failed Weddell Sea Rift System*, edited by B. C. Storey, E. C. King, and R. A. Livermore, *Geol. Soc. London, Spec. Publ.*, *108*, 45–61.

Burgess, S. D., and S. A. Bowring (2015), High-precision geochronology confirms voluminous magmatism before, during, and after Earth's most severe extinction, *Sci. Adv.*, *1*(7, e1500470), doi:10.1126/sciadv.1500470.

Burgess, S. D., S. A. Bowring, T. H. Fleming, and D. H. Elliot (2015), High-precision geochronology links the Ferrar large igneous province with early-Jurassic ocean anoxia and biotic crisis, *Earth Planet. Sci. Lett.*, *415*, 90–99, doi:10.1016/j.epsl.2015.01.037.

Caruthers, A. H., P. L. Smith, and D. R. Gröcke (2014), The Pliensbachian-Toarcian (Early Jurassic) extinction: A North American perspective, in *Volcanism, Impacts and Mass Extinctions: Causes and Effects*, *Geol. Soc. Am*., SP505, edited by G. Keller and A. Kerr, 225–243, Boulder, Colo., doi:10.1130/2014.2505(11).

Caruthers, A. H., D. R. Gröcke, and P. L. Smith (2011), The significance of an Early Jurassic (Toarcian) carbon-isotope excursion in Haida Gwaii (Queen Charlotte Islands), British Columbia, Canada, *Earth Planet. Sci. Lett.*, *307*, 19–26, doi:10.1016/j.epsl.2011.04.013.

Caruthers, A. H., P. L. Smith, and D. R. Gröcke (2013), The Pliensbachian-Toarcian (Early Jurassic) extinction, a global multi-phased event, *Palaeogeogr. Palaeoclimatol. Palaeoecol.*, *386*, 104–118, doi:10.1016/j.palaeo.2013.05.010.

Cassignol, C., and P. Y. Gillot (1982), Range and effectiveness of unspiked potassium-argon dating: Experimental groundwork and applications, in *Numerical Dating in Stratigraphy*, edited by G. S. Odin, pp. 159–179 , John Wiley, New York.

Chenet, A. L., X. Quidelleur, F. Fluteau, and V. Courtillot (2007), ^{40}K-^{40}Ar dating of the main Deccan large igneous province: Further evidence of KTB age and short duration, *Earth Planet. Sci. Lett.*, *263*, 1–15, doi:10.1016/j.epsl.2007.07.011.

Chenet, A. L., F. Fluteau, V. Courtillot, M. Gérard, and K. V. Subbarao (2008), Determination of rapid Deccan eruptions across the Cretaceous-Tertiary boundary using paleomagnetic secular variation: Results from a 1200-m-thick section in the Mahabaleshwar escarpment, *J. Geophys. Res.*, *113*, B04101, doi:10.1029/2006JB004635.

Chenet, A.-L., V. Courtillot, F. Fluteau, M. Gérard, X. Quidelleur, S. Khadri, K. V. Subbarao, and T. Thordarson (2009), Determination of rapid Deccan eruptions across the Cretaceous-Tertiary boundary using paleomagnetic secular variation: 2. Constraints from analysis of eight new sections and synthesis for a 3500-m-thick composite section, *J. Geophys. Res.*, *114*, B06103, doi:10.1029/2008JB005644.

Chevallier, L., and A. Woodford (1999), Morpho-tectonics and mechanism of emplacement of the dolerite rings and sills of the western Karoo, South Africa, *South Afr. J. Geol.*, *102*, 43–54.

Clement, B. M. (2004), Dependence of the duration of geomagnetic polarity reversals on site latitude, *Nature*, *428*, 637–640, doi:10.1038/nature02459.

Cogné, J. P. (2003), PaleoMac: A Macintosh™ application for treating paleomagnetic data and making plate reconstructions, *Geochem. Geophys. Geosyst.*, *4*(1), 1007, doi:10.1029/2001GC000227.

Coulié, E., X. Quidelleur, V. Courtillot, J.-C. Lefèvre, and S. Chiesa (2003), Comparative K-Ar and Ar/Ar dating of Ethiopian and Yemenite Oligocene volcanism: Implications for timing and duration of the Ethiopian traps, Earth Planet. *Sci. Lett.*, *206*, 477–492, doi:10.1016/S0012-821X(02)01089-0.

Coulié, E., X. Quidelleur, J.-C. Lefèvre, and P.-Y. Gillot (2004), Exploring the multicollection approach for the $^{40}Ar/^{39}Ar$ dating technique, *Geochem. Geophys. Geosyst.*, *5*, Q11010, doi:10.1029/2004GC000773.

Courtillot, V. (1994), Mass extinctions in the last 300 million years: One impact and seven flood basalts, *Israel J. Earth Sci.*, *43*, 255–266.

Courtillot, V. E., and P. R. Renne (2003), On the ages of flood basalt events, *C. R. Geosci.*, *335*, 113–140.

Courtillot, V. and F. Fluteau (2014), A review of the embedded time scales of flood basalt volcanism with special emphasis on dramatically short magmatic pulses, in *Volcanism, Impacts and Mass Extinctions: Causes and Effects*, *Geol. Soc. Am.*, SP505, edited by G. Keller and A. Kerr, pp. 301-317, Boulder, Colo., doi:10.1130/2014.2505(15).

Courtillot, V., V. A. Kravchinsky, X. Quidelleur, P. R. Renne, and D. P. Gladkochub (2010), Preliminary dating of the Viluy traps (Eastern Siberia): Eruption at the time of Late Devonian extinction events? *Earth Planet. Sci. Lett.*, *300*, 239–245, doi:10.1016/j.epsl.2010.09.045.

Courtillot, V., F. Fluteau and J. Besse (2015), Evidence for volcanism triggering extinctions: a short history of IPGP contributions with emphasis on paleomagnetism, in *Volcanism and Global Environmental Change*, edited by A. Schmidt, K. Fristad, and L. Elkins-Tanton, pp, 228–243, Cambridge Univ. Press, Cambridge, doi:10.1017/CBO9781107415683.

Cox, K. G. (1988), The Karoo province, in *Continental Flood Basalts*, edited by I. MacDougall, pp. 239–271 , Kluwer Acad, Dordrecht, Netherlands.

Dera, G., E. Pucéat, P. Pellenard, P. Neige, D. Delsate, M. M. Joachimski, L. Reisberg, and M. Martinez (2009), Water mass exchange and variations in seawater temperature in the NW Tethys during the Early Jurassic: Evidence from neodymium and oxygen isotopes of fish teeth and belemnites, *Earth Planet. Sci. Lett.*, *286*(1–2), 198–207.

Dera, G., P. Neige, J.-L. Dommergues, E. Fara, R. Laffont, and P. Pellenard (2010), High-resolution dynamics of Early Jurassic marine extinctions: The case of Pliensbachian-Toarcian ammonites (Cephalopoda), *J. Geol. Soc.*, *167*(1), 21–33.

Dera, G., B. Brigaud, F. Monna, R. Laffont, E. Pucéat, J.-F. Deconinck, P. Pellenard, M. M. Joachimski, and C. Durlet (2011), Climatic ups and downs in a disturbed Jurassic world, *Geology*, *39*(3), 215–218.

Dessert, C., B. Dupré, L. M. François, J. Schott, J. Gaillardet, G. J. Chakrapani, and S. Bajpai (2001), Erosion of Deccan traps determined by river geochemistry: Impact on the global climate and the $^{87}Sr/^{86}Sr$ ratio of seawater, *Earth Planet. Sci. Lett.*, *188*, 459–474, doi:10.1016/S0012-821X(01)00317-X.

Du Toit, A. L. (1920), The Karoo dolerites of South Africa. A study in hypabyssal injection, *Trans. Geol. Soc. S. Afr.*, *77*, 35–71.

Duncan, R. A., P. R. Hooper, J. Rehacek, J. S. Marsh, and A. R. Duncan (1997), The timing and duration of the Karoo igneous event, Southern Gondwana, *J. Geophys. Res.*, *102*(B8), 18,127–18,138, doi:10.1029/97JB00972.

Eales, H. V., J. S. Marsh, and K. G. Cox (1984), The Karoo igneous province: An introduction, in *Petrogenesis of the Volcanic Rocks of the Karoo Province*, *Spec. Publ. Geol. Soc. S. Afr*, vol. 13, edited by A. J. Erlank, pp. 1–26 .

Elliot, D. H., and T. H. Fleming (2000), Weddell triple junction: The principal focus of Ferrar and Karoo magmatism during initial breakup of Gondwana, *Geology*, *28*, 539–542, doi:10.1130/0091-7613(2000)028<0539:WTJTPF>2.3.CO;2.

Elliot, D. H., T. H. Fleming, P. R. Kyle, and K. A. Foland (1999), Long-distance transport of magmas in the Jurassic Ferrar large igneous province, Antarctica, *Earth Planet. Sci. Lett.*, *167*(1–2), 89–104, doi:10.1016/S0012-821X(99)00023-0.

Encarnacion, J., T. H. Fleming, D. H. Elliot, and H. V. Eales (1996), Synchronous emplacement of Ferrar and Karoo dolerites and the early breakup of Gondwana, *Geology*, *24*, 535–538, doi:10.1130/0091-7613(1996)024<0535:SEOFAK>2.3.CO;2.

Fiet, N., X. Quidelleur, O. Parize, L. G. Bulot, and P. Y. Gillot (2006), Lower Cretaceous stage durations combining radiometric data and orbital chronology: Towards a more stable relative time scale? *Earth Planet. Sci. Lett.*, *246*, 407–417, doi:10.1016/j.epsl.2006.04.014.

Fisher, R. A. (1953), Dispersion on a sphere, *Proc. R. Soc. London*, *217*, 295–305, doi:10.1098/rspa.1953.0064.

Fleming, T. H., A. Heimann, K. A. Foland, and D. H. Elliot (1997), $^{40}Ar/^{39}Ar$ geochronology of Ferrar Dolerite sills from the Transantarctic Mountains, Antarctica: Implications for the age and origin of the Ferrar magmatic province, *Geol. Soc. Am. Bull.*, *109*(5), 533–546, doi:10.1130/0016-7606(1997)109<0533:AAGOFD>2.3.CO;2.

Fluteau, F., and G. Le Hir (2014), Environmental changes at the K/T boundary: A geochemical numerical approach, GSA Annual Meeting, Vancouver, British Columbia.

Fuhrmann, U., H. J. Lippolt, and J. C. Hess (1987), Examination of some proposed K-Ar standards: $^{40}Ar/^{39}Ar$ analyses and conventional K-Ar data, *Chem. Geol.*, *66*, 41–51, doi:10.1016/0168-9622(87)90027-3.

Galerne, C. Y., E. R. Neumann, and S. Planke (2008), Emplacement mechanisms of sill complexes: Information from the geochemical architecture of the Golden Valley Sill Complex, *S. Afr. J. Volcanol. Geotherm. Res.*, *177*, 425–440, doi:10.1016/j.jvolgeores.2008.06.004.

Galerne, C. Y., O. Galland, E. R. Neumann, and S. Planke (2011), 3D relationships between sills and their feeders: Evidence from the Golden Valley Sill Complex (Karoo Basin) and experimental modelling, *J. Volcanol. Geotherm. Res.*, *202*, 189–199, doi:10.1016/j.jvolgeores.2011.02.006.

Ganino, C., and N. T. Arndt (2009), Climate changes caused by degassing of sediments during the emplacement of large igneous provinces, *Geology*, *37*, 323–326, doi:10.1130/G25325A.1.

Gillot, P.-Y., and Y. Cornette (1986), The Cassignol technique for potassium—Argon dating, precision and accuracy—Examples from the Late Pleistocene to recent volcanics from southern Italy, *Chem. Geol.*, *59*, 205–222.

Gillot, P.-Y., Y. Cornette, N. Max, and B. Floris (1992), Two reference materials, trachytes MDO-G and ISG_G, for argon dating (K-Ar and $^{40}Ar/^{39}Ar$) of Pleistocene and Holocene rocks, *Geostand. Newsl.*, *16*(1), 55–60.

Gillot, P.-Y., A. Hildenbrand, J.-C. Lefèvre, and C. Albore-Livadie (2006), The K-Ar dating method: Principle, analytical techniques, and application to Holocene volcanic eruptions in southern Italy, *Acta Vulcanol.*, *18*, 55–66.

Gomez, J. J., A. Goy, and M. L. Canales (2008), Seawater temperature and carbon isotope variations in belemnites linked to mass extinction during the Toarcian (Early Jurassic) in Central and Northern Spain. Comparison with other European sections, *Palaeogeogr. Palaeoclimatol. Palaeoecol*, *258*(1–2), 28–58.

Guex, J., A. Morard, A. Bartolini, and E. Morettini (2001), Découverte d'une importante lacune stratigraphique à la limite Domérien-Toarcien: Implications paléo-océanographiques, *Bull. Soc. Vaudoise Sci. Nat.*, *87*(3), 277–284.

Guex, J., A. Bartolini, J. Spangenberg, J.-C. Vicente, and U. Schaltegger (2012), Ammonoid multi-extinction crises during the Late Pliensbachian-Toarcian and carbon cycle instabilities, *Solid Earth Discuss.*, *4*, 1205–1228, doi:10.5194/sed-4-1205-2012.

Hallam, A., and P. Wignall (1997), *Mass Extinctions and Their Aftermath*, pp. 320, Oxford Univ. Press, Oxford, U. K.

Hargraves, R. B., J. Rehacek, and P. R. Hooper (1997), Palaeomagnetism of the Karoo igneous rocks in southern Africa, *S. Afr. J. Geol.*, *100*, 195–212.

Harris, C., J. S. Marsh, A. R. Duncan, and A. J. Erlank (1990), The petrogenesis of the Kirwan Basalts of Dronning Maud Land, Antarctica, *J. Petrology*, *31*, 341–369.

Heimann, A., H. T. Fleming, H. D. Elliot, and A. K. Foland (1994), A short interval of Jurassic continental flood basalt volcanism in Antarctica as demonstrated by $^{40}Ar/^{39}Ar$ geochronology, *Earth Planet. Sci. Lett.*, *121*, 19–41, doi:10.1016/0012-821X(94)90029-9.

Hermoso, M., F. Minoletti, L. Le Callonnec, H. C. Jenkyns, S. P. Hesselbo, R. E. M. Rickaby, M. Renard, M. de Rafélis, and L. Emmanuel (2009), Global and local forcing of Early Toarcian seawater chemistry: A comparative study of different paleoceanographic settings (Paris and Lusitanian basins), *Paleoceanography*, *24*, PA4208, doi:10.1029/2009PA001764.

Hermoso, M., F. Minoletti, R. E. M. Rickaby, S. P. Hesselbo, F. Baudin, and H. C. Jenkyns (2012), Dynamics of a stepped carbon-isotope excursion: Ultra high-resolution study of Early Toarcian environmental change, *Earth Planet. Sci. Lett.*, *319*, 45–54, doi:10.1016/j.epsl.2011.12.021.

Hermoso, M., F. Minoletti, and P. Pellenard (2013), Black shale deposition during Toarcian super-greenhouse driven by sea level, *Clim. Past*, *9*, 2703–2712, www.clim-past.net/9/2703/2013/, doi:10.5194/cp-9-2703-2013.

Hesselbo, S. P., D. R. Gröcke, H. C. Jenkyns, C. J. Bjerrum, P. Farrimond, H. S. Morgans Bell, and O. R. Green (2000), Massive dissociation of gas hydrate during a Jurassic oceanic event, *Nature*, *406*(6794), 392–395, doi:10.1038/35019044.

Hesselbo, S. P., H. C. Jenkyns, L. V. Duarte, and L. C. V. Oliveira (2007), Carbon-isotope record of the Early Jurassic (Toarcian) oceanic anoxic event from fossil wood and marine carbonate (Lusitanian Basin, Portugal), *Earth Planet. Sci. Lett.*, *253*, 455–470, doi:10.1016/j.epsl.2006.11.009.

Heunemann, C., D. Krsa, H. C. Soffel, E. Gurevitch, and V. Bachtadse (2004), Directions and intensities of the Earth's magnetic field during a reversal: Results from the Permo-Triassic Siberian trap basalts, Russia, *Earth Planet. Sci. Lett.*, *218*(1–2), 197–213, doi:10.1016/S0012-821X(03)00642-3.

Hofmann, C., G. Féraud, and V. Courtillot (2000), $^{40}Ar/^{39}Ar$ dating of mineral separates and whole rocks from the Western Ghats lava pile: Further constraints on duration and age of the Deccan traps, *Earth Planet. Sci. Lett.*, *180*, 13–27, doi:10.1016/S0012-821X(00)00159-X.

Iglesia Llanos, M. P. (2012), Palaeomagnetic study of the Jurassic from Argentina: Magnetostratigraphy and palaeogeography of South America, *Rev. Paléobiol. (Genève)*, *11*, 151–168.

Ikeda, M., and R. S. Hori (2014), Effects of Karoo-Ferrar volcanism and astronomical cycles on the Toarcian oceanic anoxic events (Early Jurassic), *Palaeogeogr. Palaeoclimatol. Palaeoecol.*, *410*, 134–142, doi:10.1016/j.palaeo.2014.05.026.

Ivanov, A. V., S. V. Rasskazov, G. D. Feoktistov, H. He, and A. Boven (2005), $^{40}Ar/^{39}Ar$ dating of Usol'skii sill in the south-eastern Siberian Traps Large Igneous Province: Evidence for long-lived magmatism, *Terra Nova*, *17*, 203–208, doi:10.1111/j.1365-3121.2004.00588.x.

Jarboe, N. A., R. S. Coe, P. R. Renne, J. M. G. Glen, and E. A. Mankinen (2008), Quickly erupted volcanic sections of the Steens basalt, Columbia River basalt group: Secular variation, tectonic rotation, and the Steens Mountain reversal, *Geochem. Geophys. Geosyst.*, *9*, Q11010, doi:10.1029/2008GC002067.

Jenkyns, C., H. Gröcke, R. Darren, and S. P. Hesselbo (2001), Nitrogen isotope evidence for water mass denitrification during the early Toarcian (Jurassic) oceanic anoxic event, *Paleoceanography*, *16*(6), 593–603, doi:10.1029/2000PA000558.

Jenkyns, H. C. (2010), Geochemistry of oceanic anoxic events, *Geochem. Geophys. Geosyst.*, *11*, Q03004, doi:10.1029/2009GC002788.

Jerram, D. A., and M. Widdowson (2005), The anatomy of continental flood basalt provinces: Geological constraints on the processes and products of flood volcanism, *Lithos*, *79*, 385–405, doi:10.1016/j.lithos.2004.09.009.

Johnson, M. R., C. J. Van Vuuren, W. F. Hegenberger, R. Key, and U. Shoko (1996), Stratigraphy of the Karoo Supergroup in southern Africa: An overview, *J. Afr. Earth Sci.*, *23*, 3–15, doi:10.1016/S0899-5362(96)00048-6.

Jones, D. L., R. A. Duncan, J. C. Briden, D. E. Randall, and C. MacNiocaill (2001), Age of the Batoka basalts, northern Zimbabwe, and the duration of Karoo large igneous province magmatism, *Geochem. Geophys. Geosyst.*, *2*(2), 1022, doi:10.1029/2000GC000110.

Jourdan, F., G. Féraud, H. Bertrand, A. B. Kampunzu, G. Tshoso, B. L. Gall, J.-J. Tiercelin, and P. Capiez (2004), The Karoo triple junction questioned: Evidence from $^{40}Ar/^{39}Ar$ Jurassic and Proterozoic ages and geochemistry of the Okavango dike swarm (Botswana), *Earth Planet. Sci. Lett.*, *222*, 989–1006, doi:10.1016/j.epsl.2004.03.017.

Jourdan, F., G. Féraud, H. Bertrand, A. B. Kampunzu, G. Tshoso, M. K. Watkeys, and B. L. Gall (2005), The Karoo large igneous province: Brevity, origin, and relation with mass extinction questioned by new $^{40}Ar/^{39}Ar$ age data, *Geology*, *33*, 745–748, doi:10.1130/G21632.1.

Jourdan, F., G. Féraud, H. Bertrand, and M. K. Watkeys (2007a), From flood basalts to the inception of oceanization: Example from the $^{40}Ar/^{39}Ar$ high-resolution picture of the Karoo large igneous province, *Geochem. Geophys. Geosyst.*, *8*, Q02002, doi:10.1029/2006GC001392.

Jourdan, F., G. Féraud, H. Bertrand, M. K. Watkeys, and P. R. Renne (2007b), Distinct brief major events in the Karoo large igneous province clarified by new $^{40}Ar/^{39}Ar$ ages on the Lesotho basalts, *Lithos*, *98*, 195–209, doi:10.1016/j.lithos.2007.03.002.

Jourdan, F., G. Féraud, H. Bertrand, M. K. Watkeys, and P. R. Renne (2008), The $^{40}Ar/^{39}Ar$ ages of the sill complex of the Karoo large igneous province: Implications for the Pliensbachian-Toarcian climate change, *Geochem. Geophys. Geosyst.*, *9*, Q06009, doi:10.1029/2008GC001994.

Kemp, D. B., and K. Izumi (2014), Multiproxy geochemical analysis of a Panthalassic margin record of the early Toarcian oceanic anoxic event (Toyora area, Japan), *Palaeogeogr. Palaeoclimatol. Palaeoecol.*, *414*, 332–341, doi:10.1016/j.palaeo.2014.09.019.

Kirschvink, J. L. (1980), The least squares line and plane and the analysis of palaeomagnetic data, *Geophys. J. R. Astron. Soc.*, *62*, 699–718.

Knight, K. B., S. Nomade, P. R. Renne, A. Marzoli, H. Bertrand, and N. Youbi (2004), The Central Atlantic Magmatic Province at the Triassic-Jurassic boundary: Paleomagnetic and $^{40}Ar/^{39}Ar$ evidence from Morocco for brief, episodic volcanism, *Earth Planet. Sci. Lett.*, *228*, 143–160, doi:10.1016/j.epsl.2004.09.022.

Kosterov, A. A., and M. Perrin (1996), Paleomagnetism of the Lesotho basalt, southern Africa, *Earth Planet. Sci. Lett.*, *139*, 63–78, doi:10.1016/0012-821X(96)00005-2.

Krencker, F. N., S. Bodin, R. Hoffmann, G. Suan, E. Mattioli, L. Kabiri, K. B. Föllmi, and A. Immenhauser (2014), The middle Toarcian cold snap: Trigger of mass extinction and carbonate factory demise, *Global Planet. Change*, *117*, 64–78, doi:10.1016/j.gloplacha.2014.03.008.

Kuiper, K. F., A. Deino, F. J. Hilgen, W. Krijgsman, P. R. Renne, and J. R. Wijbrans (2008), Synchronizing rock clocks of Earth history, *Science*, *320*(5875), 500–504, doi:10.1126/science.1154339.

Le Gall, B., G. Tshoso, F. Jourdan, G. Féraud, H. Bertrand, J. J. Tiercelin, A. B. Kampunzu, M. P. Modisi, J. Dyment, and M. Maia (2002), $^{40}Ar/^{39}Ar$ geochronology and structural data from the giant Okavango and related mafic dyke swarms, Karoo igneous province, northern Botswana, *Earth Planet. Sci. Lett.*, *202*, 595–606, doi:10.1016/S0012-821X(02)00763-X.

Mankinen, E. A., M. Prévot, C. S. Gromme, and R. S. Coe (1985), The Steens mountain (Oregon) geomagnetic polarity transition, 1. Directional variation, duration of episodes, and rock magnetism, *J. Geophys. Res.*, *90*, 10,393–10,416, doi:10.1029/JB090iB12p10393.

Marsh, J. S. (2002), Discussion "The geophysical mapping of Mesozoic dyke swarms in southern Africa and their origin in the disruption of Gondwana" [*J. Afr. Earth Sci.* 30 (2000) 499–513], *J. Afr. Earth Sci.*, *35*, 525–527, doi:10.1016/S0899-5362(02)00156-2.

Marsh, J. S. (2016), New evidence for the correlation of basalts of the Suurberg Group with the upper part of the Karoo basalt sequence of Lesotho, in *Origin and Evolution of the Cape Mountains and Karoo Basin*, *Regional Geol. Rev.*, edited by B. Linol, M. J. de Wit, Springer, doi:10.1007/978-3-319-40859-0_6.

Marsh, J. S., and H. V. Eales (1984), The chemistry and petrogenesis of igneous rocks of the Karoo central area, southern Africa, in *Petrogenesis of the Volcanic Rocks of the Karoo Province*, *Spec. Publ. Geol. Soc. S. Afr.*, vol. 13, edited by A. J. Erlank, pp. 27–68 .

Marsh, J. S., P. R. Hooper, J. Rehacek, A. R. Duncan, and R. A. Duncan (1997), Stratigraphy and age of Karoo basalts of Lesotho and implications for correlation within the Karoo Igneous Province, in *Large Igneous Provinces*, *Geophys. Monogr. Ser.*, vol. 100, edited by J. J. Mahoney and M. Coffin, pp. 247–272 , AGU, Washington, D. C..

McArthur, J. M., D. T. Donovan, M. F. Thirlwall, B. W. Fouke, and D. Mattey (2000), Strontium isotope profile of the early Toarcian (Jurassic) oceanic anoxic event, the duration of ammonite biozones, and belemnite palaeotemperatures, *Earth Planet. Sci. Lett.*, *179*, 269–285, doi:10.1016/S0012-821X(00)00111-4.

McClintock, M., J. S. Marsh, and J. D. L. White (2008), Compositionally diverse magmas erupted close together in space and time within a Karoo flood basalt crater complex, *Bull. Volcanol.*, *70*, 923–946, doi:10.1007/s00445-007-0178-6.

McDougall, I., and T. M. Harrison (1999), *Geochronology and Thermochronology by the $^{40}Ar/^{39}Ar$ Method*, pp. 271 , Oxford Univ. Press, New York.

McElwain, J., J. Wade-Murphy, and S. P. Hesselbo (2005), Changes in carbon dioxide during an oceanic anoxic event linked to intrusion into Gondwana coals, *Nature*, *35*, 479–482, doi:10.1038/nature03618.

McFadden, P. L., and M. W. McElhinny (1988), The combined analysis of remagnetization circles and direct observations in palaeomagnetism, *Earth Planet. Sci. Lett.*, *87*, 161–172, doi:10.1016/0012-821X(88)90072-6.

McFadden, P. L., and M. W. McElhinny (1990), Classification of the reversal test in paleomagnetism, *Geophys. J. Int.*, *103*, 725–729, doi:10.1111/j.1365-246X.1990.tb05683.x.

McFadden, P. L., R. T. Merrill, M. W. McElhinny, and S. Lee (1991), Reversals of the Earth's magnetic field and temporal variations of the dynamo families, *J. Geophys. Res.*, *96*(B3), 3923–3933, doi:10.1029/90JB02275.

McLean, D. (1985), Deccan traps mantle degassing in the terminal Cretaceous marine extinctions, *Cretaceous Res.*, *6*(3), 235–259, doi:10.1016/0195-6671(85)90048-5.

Minor, D. R., and S. B. Mukasa (1997), Zircon U/Pb and hornblende $^{40}Ar/^{39}Ar$ ages for the Dufek layered mafic intrusion, Antarctica: Implications for the age of the Ferrar large igneous province, *Geochim. Cosmochim. Acta*, *61*(12), 2497–2504, doi:10.1016/S0016-7037(97)00098-7.

Mitha, V. R. (2006), An insight into magma supply to the Karoo igneous province: A geochemical investigation of Karoo dykes adjacent to the northwestern sector of the Lesotho volcanic remnant, Rhodes University, Grahamstown, 310 pp.

Mortimer, N., D. Parkinson, J. I. Raine, C. J. Adams, I. J. Graham, P. J. Oliver, and K. Palmer (1995), Ferrar magmatic province rocks discovered in New Zealand: Implications for Mesozoic Gondwana geology, *Geology*, *23*, 185–188, doi:10.1130/0091-7613(1995)023<0185:FMPRDI>2.3.CO;2.

Moulin, M., F. Fluteau, V. Courtillot, J. Marsh, G. Delpech, X. Quidelleur, M. Gérard, and A. E. Jay (2011), An attempt to constrain the age, duration, and eruptive history of the Karoo flood basalt: Naude's Nek section (South Africa), *J. Geophys. Res.*, *116*, B07403, doi:10.1029/2011JB008210.

Moulin, M., V. Courtillot, F. Fluteau, and J. P. Valet (2012), The "van Zijl" Jurassic geomagnetic reversal revisited, *Geochem. Geophys. Geosyst.*, *13*, Q03010, doi:10.1029/2011GC003910.

Mussard, M., G. Le Hir, F. Fluteau, V. Lefebvre, and Y. Goddéris (2014), Modeling the carbon-sulfate interplays in climate changes related to the emplacement of continental flood basalts, in *Volcanism, Impacts and Mass Extinctions: Causes and Effects*, edited by G. Keller and A. Kerr, *Geol. Soc. Am.*, SP505, 339–352, Boulder, Colo., doi:10.1130/2014.2505(17).

Neumann, E.-R., H. Svensen, C. Y. Galerne, and S. Planke (2011), Multistage evolution of dolerites in the Karoo large igneous province, Central South Africa, *J. Petrol.*, *52*, 959–984, doi:10.1093/petrology/egr011.

Odin, G. S., et al. (1982), Interlaboratory standards for dating purposes, in *Numerical Dating in Stratigraphy*, edited by G. S. Odin, pp. 123–150 , John Wiley, Chichester, U. K..

Ogg, J. G., and A. G. Smith (2004), The geomagnetic polarity time scale, in *A Geologic Time Scale 2004*, edited by F. M. Gradstein, J. G. Ogg, and B. Smith, pp. 63–86 , Cambridge Univ. Press, Cambridge, U. K..

Ogg, J. G., G. Ogg, and F. M. Gradstein (2008), *The Concise Geologic Time Scale*, pp. 77 , Cambridge Univ, Press, Cambridge, U. K..

Onstott, T. C., M. L. Miller, R. C. Erwing, G. W. Arnold, and D. S. Walsh (1995), Recoil refinements: Implications for the $^{40}Ar/^{39}Ar$ dating technique, *Geochim. Cosmochim. Acta*, *59*(9), 1821–1834, doi:10.1016/0016-7037(95)00085-E.

Pálfy, J., and P. L. Smith (2000), Synchrony between Early Jurassic extinction, oceanic anoxic event, and the Karoo-Ferrar flood basalt volcanism, *Geology*, *28*, 747–750, doi:10.1130/0091-7613(2000)28<747:SBEJEO>2.0.CO;2.

Pavlov, V., F. Fluteau, R. Fetisova, A. Latyshev, L. T. Elkins-Tanton, A. V. Sobolev and N. A. Krivolutskaya (2015), Volcanic pulses in the Siberian traps as inferred from Permo-Triassic geomagnetic secular variations, in *Volcanism and Global Environmental Change*, *Geol. Soc. Am.*, SP505, edited by A. Schmidt, K. Fristad, L. Elkins-Tanton, pp. 63–78, Cambridge Univ. Press, Cambridge, UK, doi:10.1017/CBO9781107415683.007.

Prévot, M., N. Roberts, J. Thompson, L. Faynot, M. Perrin, and P. Camps (2003), Revisiting the Jurassic geomagnetic reversal recorded in the Lesotho Basalt (Southern Africa), *Geophys. J. Int.*, *155*, 367–378, doi:10.1046/j.1365-246X.2003.02029.x.

Quidelleur, X., and V. Courtillot (1996), On low-degree spherical harmonic models of paleosecular variation, *Phys. Earth Planet. Inter.*, *95*, 55–77, doi:10.1016/0031-9201(95)03115-4.

Quidelleur, X., P. Y. Gillot, V. Soler, and J. C. Lefevre (2001), K/Ar dating extended into the last millennium: Application to the youngest effusive episode of the Teide volcano (Spain), *Geophys. Res. Lett.*, *28*, 3067–3070, doi:10.1029/2000GL012821.

Rampino, M. R., and R. B. Stothers (1988), Flood basalt volcanism during the past 250 million years, *Science*, *241*(4866), 663–668, doi:10.1126/science.241.4866.663.

Rehacek, J. (1995), Chemical and paleomagnetic stratigraphy of basalts in Northern Lesotho, Karoo Province, Ph.D. thesis, 298 pp., Dep. of Geol., Wash. State Univ., Pullman.

Renne, P. R., C. C. Swisher, A. L. Deino, D. B. Karner, T. L. Owens, and D. J. de Paolo (1998), Intercalibration of standards, absolute ages and uncertainties in $^{40}Ar/^{39}Ar$ dating, *Chem. Geol.*, *145*, 117–152, doi:10.1016/S0009-2541(97)00159-9.

Renne, P. R., R. Mundil, G. Balco, K. Min, and K. R. Ludwig (2010), Joint determination of ^{40}K decay constants and $^{40}Ar^*/40K$ for the Fish Canyon sanidine standard, and improved accuracy for $^{40}Ar/^{39}Ar$ geochronology, *Geochim. Cosmochim. Acta*, *74*(18), 5349–5367, doi:10.1016/j.gca.2010.06.017.

Ricci, J., X. Quidelleur, V. Pavlov, S. Orlov, A. Shatsillo, and V. Courtillot (2013), New $^{40}Ar/^{39}Ar$ and K-Ar ages of the Viluy traps (Eastern Siberia): Further evidence for a relationship with the Frasnian-Famennian mass extinction, *Palaeogeogr. Palaeoclim. Palaeoecol.*, *386*, 531–540, doi:10.1016/j.palaeo.2013.06.020.

Riisager, J., P. Riisager, and A. K. Pedersen (2003), Paleomagnetism of large igneous provinces: Case-study from West Greenland, North Atlantic igneous province, *Earth Planet. Sci. Lett.*, *214*, 409–425, doi:10.1016/S0012-821X(03)00367-4.

Riisager, P., J. Riisager, N. Abrahamsen, and R. Waagstein (2002), New paleomagnetic pole and magnetostratigraphy of Faroe Islands flood volcanics, North Atlantic igneous province, *Earth Planet. Sci. Lett.*, *201*, 261–276, doi:10.1016/S0012-821X(02)00720-3.

Riley, T. R., and K. B. Knight (2001), Age of pre-break-up Gondwana magmatism, *Antarct. Sci.*, *13*, 99–110, doi:10.1017/S0954102001000177.

Riley, T. R., I. L. Millar, M. K. Watkeys, M. L. Curtis, P. T. Leat, M. B. Klausen, and C. M. Fanning (2004), U-Pb zircon (SHRIMP) ages for the Lebombo rhyolites, South Africa: Refining the duration of Karoo volcanism, *J. Geol. Soc.*, *161*(4), 547–550, doi:10.1144/0016-764903-181.

Riley, T. R., M. L. Curtis, P. T. Leat, M. K. Watkeys, A. R. Duncan, I. L. Millar, and W. H. Owens (2006), Overlap of Karoo and Ferrar magma types in KwaZulu-Natal, South Africa, *J. Petrol.*, *47*, 541–566, doi:10.1093/petrology/egi085.

Robock, A. (2000), Volcanic eruptions and climate, *Rev. Geophysics*, *38*, 191–219, doi:10.1029/1998RG000054.

Rodriguez, E., C. S. Morris, J. Belz, E. Chapin, J. Martin, W. Daffer, and S. Hensley (2005), An assessment of the SRTM topographic products, *Tech. Rep. JPL D-31639*, 143 pp., Jet Propul. Lab., Pasadena, Calif.

Schoene, B., K. M. Samperton, M. P. Eddy, G. Keller, T. Adatte, S. A. Bowring, S. F. R. Khadri, and B. Gertsch (2015), U-Pb geochronology of the Deccan traps and relation to the end-Cretaceous mass extinction, *Science*, *347*(6218), 182–184, doi:10.1126/science.aaa0118.

Schwarz, W. H., and M. Trieloff (2007), Intercalibration of $^{40}Ar/^{39}Ar$ age standards NL-25, HB3gr hornblende, GA1550, SB-3, HD-B1 biotite and BMus/2 muscovite, *Chem. Geol.*, *242*, 218–231, doi:10.1016/j.chemgeo.2007.03.016.

Self, S., M. Widdowson, T. Thordarson, and A. E. Jay (2006), Volatile fluxes during flood basalt eruptions and potential effects on the global environment: A Deccan perspective, *Earth Planet. Sci. Lett.*, *248*, 518–532, doi:10.1016/j.epsl.2006.05.041.

Sell, B., M. Ovtcharova, J. Guex, A. Bartolini, F. Jourdan, J.-E. Spangenberg, J.-C. Vicente, and U. Schaltegger (2014), Evaluating the temporal link between the Karoo LIP and climatic-biologic events of the Toarcian Stage with high-precision U-Pb geochronology, *Earth Planet. Sci. Lett.*, *408*, 48–56, doi:10.1016/j.epsl.2014.10.008.

Sepkoski, J. J. (1986), Phanerozoic overview of mass extinction, in *Patterns and Processes in the History of Life*, edited by D. M. Raup and D. Jablonski, Springer, Berlin.

Steiger, R. H., and E. Jäger (1977), Subcommission on geochronology: Convention on the use of decay constants in geo and cosmochronology, *Earth Planet. Sci. Lett.*, *36*, 359–362, doi:10.1016/0012-821X(77)90060-7.

Suan, G., B. Pittet, I. Bour, E. Mattioli, L. V. Duarte, and S. Mailliot (2008), Duration of the Early Toarcian carbon isotope excursion deduced from spectral analysis: Consequence for its possible causes, *Earth Planet. Sci. Lett.*, *267*, 666–679, doi:10.1016/j.epsl.2007.12.017.

Suan, G., E. Mattioli, B. Pittet, C. Lécuyer, B. Suchéras-Marx, L. V. Duarte, M. Philippe, L. Reggiani, and F. Martineau (2010), Secular environmental precursors to Early Toarcian (Jurassic) extreme climate changes, *Earth Planet. Sci. Lett.*, *290*, 448–458, doi:10.1016/j.epsl.2009.12.047.

Suan, G., et al. (2011), Polar record of Early Jurassic massive carbon injection, *Earth Planet. Sci. Lett.*, *312*, 102–113, doi:10.1016/j.epsl.2011.09.050.

Svensen, H., S. Planke, A. Malthe-Sorenssen, B. Jamtveit, R. Myklebust, T. Rasmussen Eidem, and S. S. Rey (2004), Release of methane from a volcanic basin as a mechanism for initial Eocene global warming, *Nature*, *429*(6991), 542–545, doi:10.1038/nature02566.

Svensen, H., B. Jamtveit, S. Planke, and L. Chevallier (2006), Structure and evolution of hydrothermal vent complexes in the Karoo Basin, South Africa, *J. Geol. Soc.*, *163*(4), 671–682, doi:10.1144/1144-764905-037.

Svensen, H., S. Planke, L. Chevallier, A. Malthe-Sörenssen, F. Corfu, and B. R. Jamtveit (2007), Hydrothermal venting of greenhouse gases triggering Early Jurassic global warming, *Earth Planet. Sci. Lett.*, *256*(3–4), 554–566, doi:10.1016/j.epsl.2007.02.013.

Svensen, H., S. Planke, A. G. Polozov, N. Schmidbauer, F. Corfu, Y. Y. Podladchikov, and B. Jamtveit (2009), Siberian gas venting and the end-Permian environmental crisis, *Earth Planet. Sci. Lett.*, *277*, 490–500, doi:10.1016/j.epsl.2008.11.015.

Svensen, H., F. Corfu, S. Polteau, Ø. Hammer, and S. Planke (2012), Rapid magma emplacement in the Karoo large igneous province, *Earth Planet. Sci. Lett.*, *325*, 1–9, doi:10.1016/j.epsl.2012.01.015.

Thompson, R. N., S. A. Gibson, A. P. Dickin, and P. M. Smith (2001), Early Cretaceous basalt and picrite dykes of the southern Etendeka Region, NW Namibia: Windows into the role of the Tristan Mantle Plume in Parana, Etendeka magmatism, *J. Petrol.*, *42*, 2049–2081, doi:10.1093/petrology/42.11.2049.

Valet, J.-P., A. Fournier, V. Courtillot, and E. Herrero-Bervera (2012), Dynamical similarity of geomagnetic field reversals, *Nature*, *490*, 89–93, doi:10.1038/nature11491.

Van Zijl, J. S. V., K. W. T. Graham, and A. L. Hales (1962a), The palaeomagnetism of the Stormberg lavas of South Africa 1: Evidence for a genuine reversal of the Earth's field in Triassic-Jurassic times, *Geophys. J. R. Astron. Soc.*, *7*, 23–39.

Van Zijl, J. S. V., K. W. T. Graham, and A. L. Hales (1962b), The palaeomagnetism of the Stormberg lavas of South Africa 2: The behaviour of the magnetic field during a reversal, *Geophys. J. R. Astron. Soc.*, *7*, 169–182.

Ward, P. D., J. Botha, R. Buick, M. O. De Kock, D. H. Erwin, G. H. Garrison, J. L. Kirschvink, and R. Smith (2005), Abrupt and gradual extinction among Late Permian land vertebrates in the Karoo Basin, South Africa, *Science*, *307*, 709–714, doi:10.1126/science.1107068.

Wignall, P. B. (2001), Large igneous provinces and mass extinctions, *Earth Sci. Rev.*, *53*, 1–33, doi:10.1016/S0012-8252(00)00037-4.

Zijderveld, J. D. A. (1967), A.C. demagnetization rocks—Analysis of results, in *Methods in Paleomagnetism*, edited by D. W. Collinson, K. M. Creer, and S. K. Runcorn, pp. 254–286 , Elsevier, Amsterdam.

Journal of Geophysical Research Solid Earth

Supporting Information for

Eruptive History of the Karoo lava flows and their impact on early Jurassic environmental change

M. Moulin[1], F. Fluteau[1], V. Courtillot[1], J. Marsh[2], G. Delpech[3,4], X. Quidelleur[3,4], and M. Gérard[5]

[1] Institut de Physique du Globe de Paris, Sorbonne Paris Cité, Université Paris Diderot, UMR 7154 CNRS, F-75005 Paris, France, [2] Dept of Geology, Rhodes University, P.O. Box 94, Grahamstown 6140, South Africa, [3] Université Paris-Sud, Laboratoire GEOPS, UMR8148, F-91405, France, [4] CNRS, Orsay, F-91405; France, [5] IMPMC, Université Pierre et Marie Curie, IRD, F-75005 Paris, France

Contents of this file

Table S1

Introduction

This supporting information provides $^{40}Ar/^{39}Ar$ data.

Table S1. $^{40}Ar/^{39}Ar$ data
Step#: incremental heating step number; $^{40}Ar/^{39}Ar$, $^{38}Ar/^{39}Ar$, $^{37}Ar/^{39}Ar$, $^{36}Ar/^{39}Ar$: isotopic ratios; ^{39}Ar: ^{39}Ar signal (in 10^{12} mol); $\%^{40}Ar^*$: radiogenic ^{40}Ar content (in per cent); Un.: 1σ analytical uncertainties. Ages relative to FCTs=28.201 Ma [*Kuiper et al*., 2008] and *Steiger and Jaeger* [1977] decay constants.

Table S1. $^{40}Ar/^{39}Ar$ data

	Step #	T (°C)	$^{40}Ar/^{39}Ar$	$^{38}Ar/^{39}Ar$	$^{37}Ar/^{39}Ar$	$^{36}Ar/^{39}Ar$	^{39}Ar (10^{-12}.mol)	% ^{40}Ar*	$^{40}Ar^*/^{39}Ar_K$	Un.	Age (Ma)	Un. (Ma)	Cl/K	Un.	Ca/K	Un.
MP05-09																
J=0.01464																
	1	520	9,510	0,0314	18,11	0,00982	0,22518	84,6	8,150	0,187	203,3	4,4	0,0052	0,0018	37,06	0,41
	2	630	7,719	0,0107	22,29	0,00743	0,75275	94,4	7,407	0,112	185,7	2,7	-0,0005	0,0009	45,76	0,46
	3	680	7,366	0,0086	24,09	0,00763	1,83592	95,3	7,141	0,084	179,4	2,0	-0,0010	0,0003	49,51	0,50
	4	730	7,317	0,0110	23,36	0,00714	1,74731	96,4	7,177	0,082	180,3	2,0	-0,0003	0,0001	47,99	0,48
	5	780	7,320	0,0135	22,44	0,00713	1,89964	95,5	7,105	0,080	178,5	1,9	0,0004	0,0001	46,07	0,46
	6	825	7,353	0,0179	21,79	0,00628	0,71459	98,2	7,337	0,089	184,1	2,1	0,0016	0,0005	44,73	0,45
	7	870	7,406	0,0130	20,11	0,00637	0,78192	96,1	7,220	0,081	181,3	1,9	0,0002	0,0009	41,21	0,41
	8	915	7,485	0,0197	17,47	0,00546	0,52243	96,9	7,347	0,102	184,3	2,4	0,0021	0,0019	35,73	0,37
	9	955	7,471	0,0184	14,95	0,00516	0,4276	95,4	7,208	0,108	181,0	2,6	0,0017	0,0006	30,53	0,32
	10	995	7,853	0,0398	19,60	0,00649	0,09791	95,3	7,595	0,349	190,2	8,3	0,0077	0,0067	40,17	0,56
	11	1130	7,551	0,0089	23,42	0,00739	0,3152	95,6	7,346	0,103	184,3	2,5	-0,0009	0,0006	48,12	0,50
	12	1250	7,642	0,0191	25,14	0,00796	0,5554	95,3	7,415	0,107	185,9	2,6	0,0019	0,0006	51,72	0,53
MP07-09																
J=0.01465																
	1	520	11,955	-0,0325	18,39	0,02288	0,04991	55,6	6,738	1,254	169,8	30,2	-0,0134	0,0087	37,65	0,90
	2	630	8,033	0,0107	34,99	0,01343	0,86231	85,1	7,010	0,163	176,4	3,9	-0,0006	0,0006	72,51	0,73
	3	680	7,467	0,0059	35,26	0,01114	1,08986	93,3	7,147	0,144	179,6	3,4	-0,0018	0,0008	73,09	0,73
	4	730	7,414	0,0154	35,06	0,01122	1,02797	92,7	7,053	0,155	177,4	3,7	0,0009	0,0005	72,66	0,73
	5	780	7,415	0,0136	32,56	0,01046	1,72142	93,1	7,068	0,134	177,7	3,2	0,0004	0,0002	67,35	0,67
	6	825	7,427	0,0175	30,19	0,00865	0,25889	97,8	7,423	0,199	186,2	4,8	0,0015	0,0015	62,33	0,65
	7	915	7,537	0,0208	27,83	0,00865	0,45267	95,3	7,330	0,171	184,0	4,1	0,0024	0,0021	57,36	0,58
	8	1070	7,582	0,0105	32,06	0,01039	0,70996	93,0	7,216	0,144	181,3	3,5	-0,0005	0,0009	66,30	0,67
	9	1250	7,930	0,0150	35,05	0,01286	1,01348	87,1	7,085	0,159	178,2	3,8	0,0007	0,0005	72,62	0,73
NN45																
J=0.01434																
	1	520	30,605	0,0286	10,26	0,07781	0,04945	27,5	8,487	2,190	207,2	50,5	0,0007	0,0224	20,88	0,47
	2	630	7,908	0,0128	16,23	0,00516	1,10078	97,0	7,759	0,092	190,3	2,2	0,0002	0,0003	33,16	0,33
	3	670	7,495	0,0181	18,26	0,00548	1,78448	97,7	7,420	0,080	182,4	1,9	0,0017	0,0004	37,38	0,37
	4	710	7,482	0,0127	16,13	0,00497	2,4306	97,4	7,374	0,064	181,3	1,5	0,0002	0,0002	32,96	0,33
	5	750	7,507	0,0116	13,91	0,00419	1,20019	98,2	7,445	0,069	183,0	1,6	-0,0001	0,0004	28,37	0,28
	6	790	7,564	0,0096	12,53	0,00277	0,30656	102,3	7,806	0,087	191,4	2,0	-0,0007	0,0028	25,53	0,28
	7	825	7,615	0,0139	10,48	0,00252	0,29536	101,1	7,759	0,124	190,3	2,9	0,0005	0,0025	21,33	0,25
	8	915	7,568	0,0137	7,87	0,00213	0,43967	99,9	7,605	0,098	186,7	2,3	0,0005	0,0012	15,99	0,19
	9	1070	7,593	0,0144	19,69	0,00566	0,37335	98,5	7,586	0,107	186,3	2,5	0,0007	0,0015	40,35	0,42
	10	1250	8,572	0,0130	25,19	0,01050	0,52449	87,1	7,603	0,133	186,7	3,1	0,0001	0,0008	51,82	0,53
NN57																
J=0.01449																
	1	630	8,138	0,0131	9,16	0,00407	0,58503	94,1	7,712	0,095	191,1	2,2	0,0002	0,0013	18,63	0,19
	2	690	7,600	0,0089	8,91	0,00238	0,5435	100,0	7,650	0,076	189,7	1,8	-0,0009	0,0009	18,12	0,20
	3	750	7,576	0,0150	8,75	0,00244	0,42292	99,6	7,596	0,141	188,4	3,3	0,0008	0,0015	17,79	0,22
	4	805	7,611	-0,0041	7,97	0,00242	0,21241	98,9	7,571	0,082	187,8	1,9	-0,0045	0,0030	16,20	0,25
	5	915	7,652	0,0323	5,34	0,00170	0,24017	99,0	7,601	0,109	188,5	2,6	0,0056	0,0039	10,84	0,17
	6	1070	7,766	0,0230	12,44	0,00427	0,23971	96,4	7,557	0,153	187,5	3,6	0,0030	0,0031	25,36	0,34
	7	1250	8,921	-0,0129	19,39	0,01004	0,13539	84,0	7,595	0,276	188,4	6,5	-0,0072	0,0053	39,71	0,45

[a] Step#: incremental heating step number; $^{40}Ar/^{39}Ar$, $^{38}Ar/^{39}Ar$, $^{37}Ar/^{39}Ar$, $^{36}Ar/^{39}Ar$: isotopic ratios; ^{39}Ar: ^{39}Ar signal (in 10^{12} .mol); %$^{40}Ar^*$: radiogenic ^{40}Ar content (in per cent); Un.: 1σ analytical uncertainties. Ages relative to FCTs=28.201 Ma [*Kuiper et al.*, 2008] and *Steiger and Jaeger* [1977] decay constants.